The Pennsylvania State University
The Graduate School

STATISTICAL ANALYSIS OF CONVECTIVE UPDRAFTS IN TROPICAL CYCLONE RAINBANDS OBSERVED BY AIRBORNE RADAR

A Thesis in
Meteorology and Atmospheric Science
by
Nicholas R. Barron

Submitted in Partial Fulfillment
of the Requirements
for the Degree of

Master of Science

December 2020

The thesis of Nicholas R. Barron was reviewed and approved by the following:

Anthony C. Didlake Jr.
Assistant Professor of Meteorology
Thesis Advisor

George S. Young
Professor of Meteorology

Kelly Lombardo
Associate Professor of Meteorology and Atmospheric Science

James H. Ruppert Jr.
Assistant Research Professor

David J. Stensrud
Department Head and Professor of Meteorology

Abstract

Ten years of airborne Doppler radar observations are used to study the kinematic and reflectivity structures of convective updrafts in tropical cyclone (TC) rainbands. An automated algorithm is developed to identify the strongest rainband updrafts across 12 TCs. The selected updrafts are then collectively analyzed by their frequency, radius, azimuthal location (relative to the 200-850 hPa environmental wind shear), structural characteristics, and secondary circulation (radial/vertical) flow pattern. Rainband updrafts become deeper and stronger with increasing radius. A wavenumber-1 asymmetry arises showing that in the downshear (upshear) quadrants of the TC, updrafts are more (less) frequent and deeper (shallower). Low-level radial flows near the updrafts correspond to the background vortex-scale radial flow asymmetry, being predominantly inflow (outflow) in the downshear (upshear) quadrants. Moreover, the downshear inflow layer decreases in depth traveling from the downshear-right to downshear-left quadrants. In the right-of-shear quadrants, updrafts tend to have either in-up-out or in-up-in secondary circulation patterns, with the in-up-out circulation generally having the deepest updraft and reflectivity tower. In the downshear-left quadrant, the dominant updraft circulation type shifts from primarily in-up-out to out-up-out. It is hypothesized that this shift is due to the decrease in radial inflow layer depth, the bottom-up decay of older updrafts, and the increase in stratiform precipitation surrounding the updrafts. In particular, the stratiform region encourages cold-pool dynamics that support new convective updrafts with a preferred out-up-out circulation. The findings presented in this study support the previous literature regarding organized rainband convection in a mature and sheared TC.

Table of Contents

List of Figures

List of Tables

Acknowledgments

First, I would like to express my immense gratitude for my wife, Shelby Barron. Her unconditional love and support have helped me get through some of the challenging components of assembling this document. It should go without saying, but I could not have done it without her. Mark and Faith Barron, my parents, have given me the tools of cynicism and critical thinking. I can never thank them enough for the years of parenting that have made me who I am today.

Second, I would like to thank my thesis advisor, Anthony Didlake. I am incredibly thankful that he has given me the opportunity to work with, and learn from, him. His insight, dedication, and teaching have helped me to become a better researcher and communicator. I, also, could not have done this without him.

I would also like to thank my master's committee members: George Young, Kelly Lombardo, and James Ruppert. Their wise comments, careful review, and critique of the manuscript have been an immense boon to the quality and readability of the content therein.

Lastly, I want to thank my undergraduate advisor at Cleveland State University, Thijs Heus. Without the research opportunities that he offered me, I would have never become exposed to atmospheric science and meteorology in the first place. If my parents were the ones that instilled the cynical and explorative forces that drove my thoughts as a student, Thijs was the fulcrum that allowed those forces to do work. The result of this interaction created an imbalance that changed the entire trajectory of my career, placing me on the path that I am on today.

This material is based upon work supported by the National Science Foundation under Award No. AGS-1810869. Any opinions, findings, and conclusions or recommendations expressed in this publication are those of the author(s) and do not necessarily reflect the views of the National Science Foundation.

Chapter 1
Introduction

Spiral rainbands are ubiquitous features in tropical cyclones (TCs) that constitute much of the area and total precipitation of the overall TC. These convection features can involve complex interactions with the boundary layer (e.g., Yu and Chen 2011; Li and Dai 2020; Ren et al. 2020), eyewall (e.g., Chen and Yau 2001; Li et al. 2015; Wadler et al. 2018), and surrounding environment (e.g., Riemer and Montgomery 2011; Didlake and Houze 2013b; Dai et al. 2019), potentially leading to significant impacts on TC evolution. Rainbands can act as a local source of potential vorticity (PV) that spirals into the PV central core, which can help strengthen the storm (Judt and Chen, 2010; Yu and Chen, 2011; Li and Dai, 2020). Oppositely, weakening can occur when rainband downdrafts reduce the θ_e of boundary layer air feeding into the eyewall (Powell, 1990a,b; Sawada and Iwasaki, 2010a,b; Yu and Chen, 2011; Li and Wang, 2012a,b; Li and Dai, 2020). Rainbands can also alter the TC structure either by accelerating the local tangential winds and expanding the TC wind field (Smith et al., 2009; Bu et al., 2017), or by contributing to the development of a secondary eyewall outside of the pre-existing primary eyewall (Willoughby et al., 1982; Didlake and Houze, 2011; Rozoff et al., 2012; Yu and Didlake, 2019). The overall role of rainbands in TC evolution has not yet been completely understood, in part due to an insufficient understanding of the different rainband structures and processes that can occur in nature. The current study addresses this gap in knowledge by exploring the detailed structures of observed rainband convection.

Rainbands can exist in a wide variety of manners, with differing spatial structures and temporal evolution at all stages of a TC's lifetime. Despite such variety, rainbands often exhibit repeated patterns in location, composition, and behavior due to large-scale environmental factors. One such factor is vertical, deep-layer (200-850 hPa), environmental wind shear. In the presence of sufficient deep-layer environmental wind

shear, TC rainbands are organized into a broad, asymmetric complex termed the Stationary Band Complex (SBC; Willoughby et al. 1984). Right of the deep-layer shear vector, the SBC exhibits discrete or connected convective cells that grow and mature as they propagate downwind. These cells generally exhibit low-level radial inflow that turns upward into intense buoyant updrafts, then turns radially outward in the mid-troposphere (5-8 km) (Barnes et al., 1983; Powell, 1990a,b; Samsury and Zipser, 1995; Hence and Houze, 2008). This flow pattern can build local tangential wind jets through stretching and tilting of the background vorticity field. The convective cells also contain two distinct downdrafts: a low-level downdraft originating at 2-4 km altitude driven by precipitation drag, and an inner-edge downdraft originating at 6-8 km altitude formed along the inner boundary of the rainband (Didlake and Houze, 2009). Traveling downwind into the left-of-shear half of the TC, the rainband convection weakens and collapses into a broad, homogeneous band of predominantly stratiform precipitation. In this downwind stratiform rainband, Didlake and Houze (2013b) and Didlake et al. (2018) found mesoscale descending radial inflow that was forced by latent cooling within the stratiform precipitation that extended into the boundary layer. Modeling studies show that this mesoscale downdraft forms a cold pool that can trigger and maintain new convective updrafts embedded in the larger stratiform band (Yu and Didlake, 2019; Li and Dai, 2020; Yu et al., 2020).

Rainband convection also varies with radius from the storm center, due to the radially changing influences of the vortex circulation and surrounding environment. Convective updrafts at a smaller radius generally extend to a lower altitude than those farther from the storm center (Li and Wang, 2012a; Didlake and Houze, 2013a). This may be due to decreasing convective available potential energy for buoyant updrafts at smaller radii (Bogner et al., 2000; Molinari et al., 2012; Li and Fang, 2019) or rapid filamentation and dissipation of convective elements due to strong horizontal wind shear in inner core regions (Rozoff et al., 2006). Distant rainbands, located far from the storm center, are buoyancy-driven convective elements that propagate outward in a manner similar to squall lines with a locally generated cold pool (Tang et al., 2014; Moon and Nolan, 2015). Just outside the eyewall of a mature TC, rainbands often behave as convectively-coupled vortex-Rossby waves that propagate along the radial vorticity gradient of a TC vortex (e.g., Montgomery and Kallenbach 1997; Wang 2002; Corbosiero et al. 2006; Li and Wang 2012a; Li et al. 2017).

Many previously mentioned observational and modeling studies involve case examinations of one or a small number of storms (e.g., Barnes and Stossmeister 1986; Barnes

et al. 1991; Didlake and Houze 2013a,b; Tang et al. 2014; Moon and Nolan 2015; Tang et al. 2018). Unfortunately, such case studies do not individually capture the full variety of rainband features that occur in nature. In contrast, other studies may examine the inner core structures in a large number of TCs (e.g., Reasor et al. 2013; Rogers et al. 2013). However, these studies usually use azimuthally-averaged profiles to analyze behaviors within the rainband which potentially obscure smaller-scale rainband features important for examining the full TC evolution. There are a few TC studies that capture the details of convective-scale features across multiple TC cases. Wadler et al. (2018) tracked individual convective bursts that initiated near the eyewall in multiple observed storms and they determined the frequency, location, and burst characterizations that were most important for rapid intensification of the TC. Using ground-based radar observations, Yu et al. (2018) found that TC outer rainbands were more likely to develop squall-line-like characteristics. Terwey and Rozoff (2014) developed an automated updraft tracking algorithm specifically for use with numerical simulations and applied it successfully to two different models; they found notable differences between the models in updraft frequencies, structures, and evolution. Li and Fang (2019) also used model simulations to study the buoyancy of convective updrafts and found that updraft buoyancy is significantly larger in the downshear half of the TCs. These studies successfully track and examine some aspects of individual convective updrafts. The current study seeks to extend the prior work by using a similar tracking methodology in an observations-based analysis of a large quantity of rainband structures analyzing a wider scope of updraft features.

In this study, we analyze the convective-scale structures of TC rainbands captured by 10 years' worth of airborne Doppler radar observations from Atlantic and east Pacific basin hurricanes. In particular, we focus on convective rainband updrafts and their associated convective-scale kinematic and reflectivity structures. We first identify the strongest rainband updrafts in each storm, then statistically analyze their specific characteristics, including their frequency, radial location, shear-relative location, depth, strength, and secondary circulation flow pattern. The result is an improved understanding of the variety of observed rainband updraft structures across a variety of hurricane-strength TCs. A brief overview of the observational data and methods is presented in Chapter 2. In Chapters 3 and 4, we investigate how updraft size and location vary with radius and shear-relative azimuth. In Chapter 5, the secondary circulation around each updraft is investigated. This includes an analysis of shear-relative quadrant composites, and the development and application of an objective updraft circulation classification algorithm.

The conclusions for this study are in Chapter 6.

Chapter 2
Data and Methods

2.1 Airborne radar observations

The airborne observations used for this study were obtained by the National Oceanic and Atmospheric Administration (NOAA) WP-3D (P3) Tail Doppler radar (TDR). The P3 TDR is an X-band (3.2 cm) Doppler radar with two antenna pointed 20° fore and aft that provide two nearly simultaneous independent measurements of a single arbitrary region. With this scanning strategy, the three-dimensional velocity field can be retrieved in regions up to ± 50 km from the radar (Lorsolo et al., 2013). The data for this study are from 59 missions across 12 hurricane-strength ($\geq$ 33 ms^{-1}) TCs in the Atlantic and east Pacific basins, spanning from 2010 to 2019 (see Table 2.1 for a comprehensive list). The TC maximum wind speeds are taken from the NOAA National Hurricane Center HURDAT2 dataset (Landsea and Franklin, 2013), providing wind speeds at 6-hour intervals during the lifetime of each TC. These intensities are then interpolated to the middle time of each mission. Most missions performed nominal survey patterns that consisted of multiple radial passes through the eyewall that optimized azimuthal coverage of the storm.

The radar observations were first analyzed with an automated quality control and dealiasing algorithm successfully applied in other studies using TDR data (e.g., Rogers et al. 2012; Reasor et al. 2013; Fischer et al. 2019). 3D velocity vectors were then retrieved using a variational technique that constrains and optimizes the radar projection equation along with mass continuity and boundary conditions (Gamache, 1997; Gao et al., 1999; Reasor et al., 2009). The retrieval then maps the reflectivity and velocity fields onto a Cartesian grid with horizontal spacing of 2 km and vertical spacing of 0.5 km. Storm

vortex centers were determined using a real-time analysis of flight level data (Willoughby and Chelmow, 1982). The average storm motion for each mission was subtracted from the wind retrievals to obtain the storm-relative velocity field in all subsequent analyses. These data were then interpolated to a storm-centered cylindrical coordinate system with grid spacing of 2 km $\times 2^\circ \times 0.5$ km in the radial, azimuthal, and vertical directions. Finally, to account for varying storm sizes, the radial coordinate of each updraft is normalized by the radius of maximum wind, here defined to be the azimuthally-averaged 2 km tangential wind maximum for each mission.

2.2 Updraft selection and updraft properties

Using the retrieved velocity fields for each radial pass, individual convective rainband updrafts were selected by the following procedure. First, vertical velocity thresholds were defined for each mission by analyzing the distribution of all vertical velocities in a given mission at 2 km altitude and at radii larger than $1.5r^*$, where r^* is the radius of maximum wind. The average r^* is approximately 45 km, and the first and third quartiles of the r^* distribution are 25 and 50 km radius, respectively. The threshold for that mission was set at the 95th percentile of the vertical velocity distribution (see Table 2.1 for values). We used this percentile method to account for inherent variability across all missions. Next, convective updrafts were defined by clustering all connected data pixels where the vertical velocity was greater than the vertical velocity threshold; this process will form a 3D boundary around each updraft element. In order to prevent the inclusion of dubious updraft elements (i.e., apparent updrafts suspected to have notable errors in the retrieval solution), selected updrafts must also pass several other tests. Geometrically, updraft elements must include at least 2 horizontal grid points or 4 vertical grid points. To evaluate and refine the convective nature of selected updrafts, we applied a convective-stratiform classification algorithm on the reflectivity field (Steiner et al., 1995; Didlake and Houze, 2009) and determined the fraction of the vertical-velocity-defined updraft element that is convectively classified. Updrafts with 40% or more convectively-classified pixels are included in the analysis. This value was found to produce an optimal balance of maximizing updraft quantities while also reducing the inclusion of stratiform elements. Fig. 2.1 shows an example of selected updraft elements in Hurricane Matthew overlaid on 2-km altitude vertical velocity and reflectivity fields. The radial, azimuthal, and vertical locations of each updraft element are defined by the vertical-velocity-weighted centroid.

Table 2.1. Storm name and aircraft mission ID for the tail Doppler radar data used in this study. Given for each mission are the number of eyewall passes made, number of convective updrafts selected, 200-850 hPa wind shear magnitude and direction (meteorological azimuth of vector arrow), maximum wind speed of the TC, and vertical velocity threshold for updraft selection. The naming format for the missions are YYMMDDAN, where "YY" is the year, "MM" is the month, "DD" is the day of the month, "A" is the aircraft, and "N" is the mission number for that aircraft on a given day. The missions marked with a "*" have a mature secondary eyewall. The mission marked with a "+" are east Pacific storms, and the remaining are Atlantic basin storms.

Storm name and mission ID	Num. passes	Num. updrafts	Sh. Mag. (ms^{-1})	Sh. Dir °	Max winds (ms^{-1})	Threshold (ms^{-1})
EARL: 100829I1	4	43	2.4	146.7	42.6	1.14
EARL: 100830H1	3	40	6.6	26.4	54.4	0.89
EARL: 100830I1	3	28	5.7	243.9	59.2	1.49
EARL: 100901H1	2	34	6.7	47.3	56.4	0.9
EARL: 100901I1	2	36	10.6	55.9	62	1.35
EARL: 100902H1*	3	36	10.1	34.1	60.1	1.13
ARTHUR: 140703I1	1	10	10.4	54.2	42.2	1.22
EDOUARD: 140914I1	3	9	6.6	45.6	37.8	1.12
EDOUARD: 140915H1	2	19	8.5	94.9	48.5	1.13
EDOUARD: 140915I1	2	14	7.7	89.3	48.3	1.21
EDOUARD: 140916H1*	2	16	8.8	86.2	50.8	0.99
EDOUARD: 140916I1	2	1	9.6	83	47.7	1.37
EDOUARD: 140917H1	2	4	13.1	53.2	41.2	1.01
GONZALO: 141016I1	2	2	7.3	356.2	64	1.37
GONZALO: 141017I1*	2	1	7.2	54.6	56.5	1.37
MATTHEW: 160930I1	2	20	16.8	19	60.3	0.84
MATTHEW: 161001I1*	2	5	13.7	31.3	67.1	1.02
MATTHEW: 161005I1	3	1	10.7	319.9	54.4	0.76
MATTHEW: 161005I2	3	12	7.8	345.6	54	0.71
MATTHEW: 161006I2*	5	89	9.1	12.8	60	0.85
MATTHEW: 161007I1	1	20	7.8	37.4	51.2	1.34
HARVEY: 170824H2	3	35	1.9	58.5	36.4	0.57
HARVEY: 170825H1	3	29	11	329.7	45.6	0.61
HARVEY: 170825H2	2	18	5.7	32.3	53.7	0.8
IRMA: 170903H1	3	18	3.3	179.1	51.4	0.62
IRMA: 170904H1*	4	59	6.3	165.6	56.2	0.76
IRMA: 170904H2	3	16	4.2	219.3	63.5	0.8
IRMA: 170905H1	3	25	4.6	341.9	75.9	0.81
IRMA: 170905H2	4	34	3	234.5	79.7	0.76
IRMA: 170908H1*	4	12	8.3	178.8	69.6	0.58
IRMA: 170908H2	3	8	4.8	112.2	73.9	0.47
MARIA: 170922H1	3	10	16	36.2	55.4	1.05
MARIA: 170923H1*	3	9	12.3	243	51.4	0.89
MARIA: 170924H1	4	34	11.4	19.6	48.9	0.58
NATE: 171007H1	4	19	4.2	340.6	40.3	0.68
LANE: 180820H1+	3	24	10.6	18.9	56.5	0.68
LANE: 180820H2+	3	21	10.7	21.8	59	0.77
LANE: 180821H1+	4	29	9.7	26.1	66.3	0.56
LANE: 180822H1+	3	39	6.3	50.6	71.8	0.52
FLORENCE: 180909H1	3	37	11.2	15.9	34.9	0.59
FLORENCE: 180910H1	4	27	7.6	183.9	60.4	0.61
MICHAEL: 181008H1	3	21	14	0.2	43.5	0.67
MICHAEL: 181009H1	5	45	13.3	200.1	46.5	0.6
MICHAEL: 181009H2	5	44	11.6	331.7	57.1	0.55
MICHAEL: 181010H1	3	28	9	316.3	64.1	0.69
DORIAN: 190828H1	3	14	5.7	300	38.1	0.57
DORIAN: 190829H1	4	48	7.3	302.2	38.6	0.87
DORIAN: 190829H2	3	38	5.1	290	42	0.81
DORIAN: 190830H1	4	30	6.9	303.2	49.6	0.9
DORIAN: 190830H2	3	43	5.6	320.9	58.9	0.82
DORIAN: 190831H1	5	43	7.7	318.7	64.7	0.87
DORIAN: 190831H2	4	31	7.9	346.9	70.1	0.8
DORIAN: 190901H1	3	30	9.8	341	81.1	0.56
DORIAN: 190902H2	5	37	7	347	59.8	0.98
DORIAN: 190903H1	5	30	6.6	314.4	51.8	0.73
DORIAN: 190904H1	6	25	8.9	71.1	51	0.62
DORIAN: 190905H1	8	13	7.3	99	51	0.74
DORIAN: 190905H2	8	15	10.3	35.3	46.5	0.57

In order to exclude the eyewall and distant rainbands from our analysis, only updrafts positioned greater than $2r^*$ and less than $9r^*$ are included. Azimuthal locations are measured relative to the pointing directions of two vectors: the storm motion vector and the deep-layer environment shear vector, each with azimuth increasing clockwise. The storm motion (or storm track) vector is calculated by measuring the differential distance between vortex center positions at every 20 minutes, and then dividing by the time between those data points. These measurements are then interpolated to the time of each eyewall pass. The deep-layer (200-850 hPa) environmental wind shear vector is calculated from the National Center for Environmental Prediction global reanalysis-2 dataset using the vortex-removal procedure detailed in Davis et al. (2008). In this procedure, the irrotational and nondivergent components of the wind are subtracted from the 200 and 850 hPa horizontal wind fields. The remaining background flow is averaged over a disk extending out to 800 km from the storm center to produce two vectors; the 850 hPa vector is then subtracted from the 200 hPa vector to yield the deep-layer shear vector.

In storms where a secondary eyewall is present or imminent, we aimed to count only updrafts in rainbands, and not those in mature secondary eyewalls. Our approach first defines a "mature" secondary eyewall as any local maximum in the 0.5-2 km layer average axisymmetric tangential wind that has a corresponding quadrant local maximum in at least 3 shear-relative quadrants. If one is identified, and the location of the secondary eyewall is greater than $2r^*$, the selected updrafts must be radially outside the mature secondary eyewall. In this manner, we still include observations of storms with a developing, but not mature, secondary eyewall.

The normalized radius, shear-relative azimuth (θ_s), and track-relative azimuth (θ_t) describe the location of each updraft. Additional characteristics for each updraft are the updraft base, top, depth, and strength. The updraft base and top describe the lowermost and uppermost altitudinal positions of an updraft element. Updraft depth is the difference between the top and base altitudes. Finally, the updraft strength is defined as the maximum vertical velocity within the updraft.

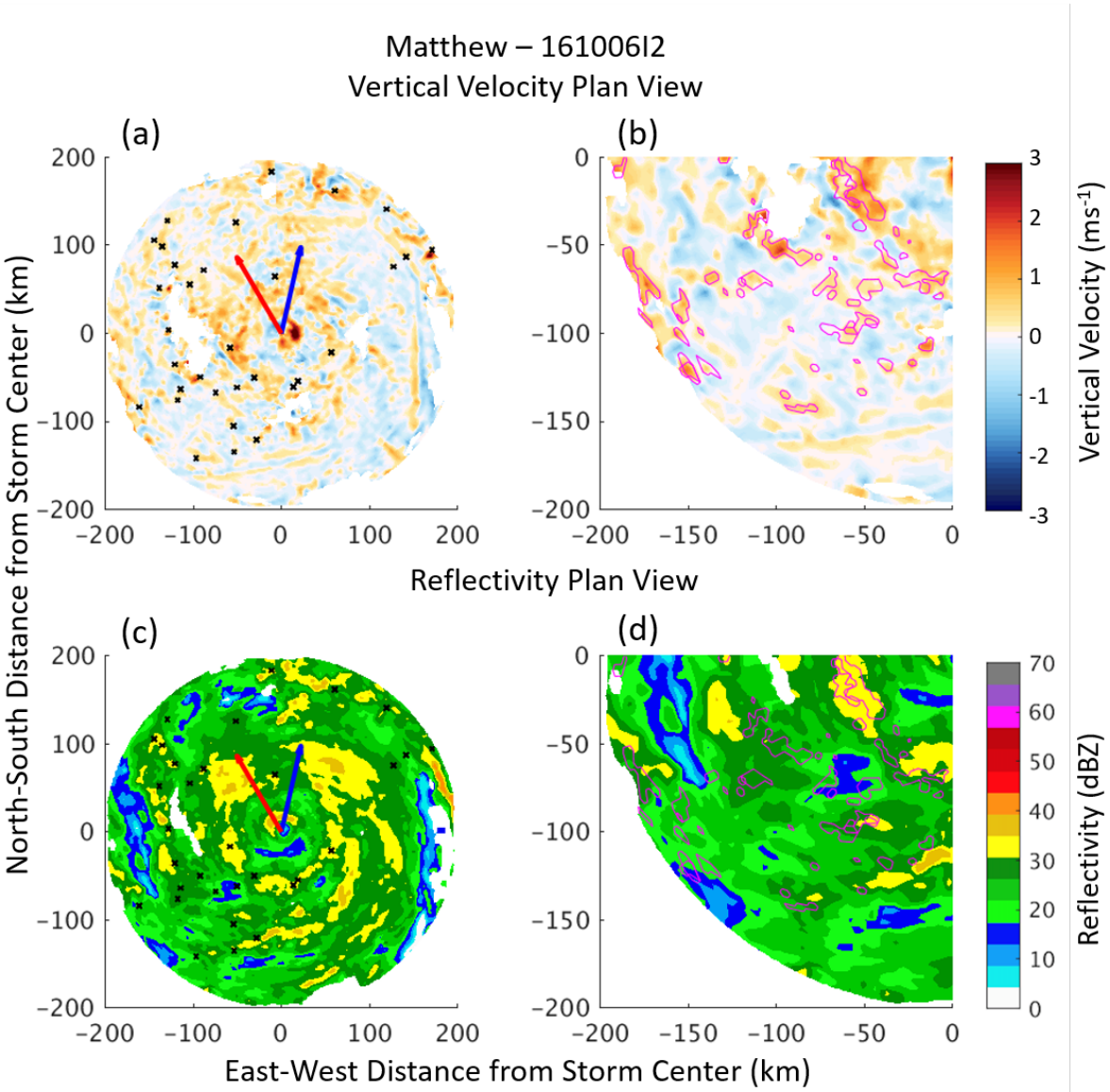

Figure 2.1. Plan view showing convective updraft locations overlaid on (a,b) vertical velocity and (c,d) reflectivity at 2 km altitude from Hurricane Matthew mission 161006I2. At this time, Matthew had maximum winds of 61 ms^{-1}. Shown in (a) and (c) are full plan views with black crosses denoting convective updraft horizontal locations. Blue and red arrows are the environmental shear and storm track vectors, respectively. Shown in (b) and (d) are plan views zoomed in on the southwest quadrant with convective updraft horizontal extent outlined in magenta.

Chapter 3
Updraft size, strength, and location in an axisymmetric framework

In this chapter, we analyze the distributions of the updraft characteristics with respect to the normalized radius r^*; this analysis essentially collapses the statistics into an axisymmetric framework. Figure 3.1 shows the joint frequency distributions of updraft normalized radius vs. updraft base altitude, top altitude, depth, and strength.

Overall, the frequency of updrafts increases with decreasing radius, as shown by the single-dimension frequency distribution. Seen in Fig. 3.1a, the updraft base altitude does not change appreciably with radius. The base altitude shows two regimes of modes at 1-2 km and 0-1 km base altitude at 2-4r^* and 4-6r^*, respectively. Most of the base altitudes are below 3 km. A peaked distribution of base altitudes is present at 2-4r^*, then the distribution flattens at larger radii. Beyond 6r^*, updraft counts decrease significantly, but a mode between 1-2 km is still found. In Fig. 3.1b, the updraft top heights are largely above 6 km altitude and have distribution modes between 6-12 km. The distribution structure changes with respect to radius. Between 2-4r^*, a wide distribution is displayed with a mode occurring between 6-8 km. Between 4-5r^*, the mode shifts to higher altitudes (at 8-10 km). At 5-6r^*, a bimodal distribution emerges, with local frequency maxima at 6-8 km and 10-12 km. The updraft depths in Fig. 3.1c, show a slight trend of deeper updrafts with increasing radius. At smaller radii (2-4r^*), the mode is between 4-6 km and the distribution has a broad tail with a notable number of updrafts growing as deep as 12 km. Between 4-6r^*, the depth mode increases to 6-8 km. Figure 3.1d shows that the updraft strength is often between 1-2 ms^{-1}. At larger radii (4-6r^*), the 1-2 ms^{-1} and 2-3 ms^{-1}

updrafts occur at similar frequencies, unlike those updrafts at smaller radii. This shift in the distribution indicates that the updrafts at larger radii are more likely to be stronger than the those at smaller radii, which is consistent with our previous finding of increasing depths with radius.

These findings have some consistency with previous observations of TC rainbands. Didlake and Houze (2013a) showed that, from a single case study, rainband convective updrafts at larger radii had greater depths, vertical velocity magnitudes, and tops than those at smaller radii. Our results reflect these same kinematic findings (within 2-6r^*) across many storms. The primary causative factor for these convective radial variations is a general increase in Convective Available Potential Energy (CAPE) with larger radius (Bogner et al., 2000; Molinari et al., 2012). Hence and Houze (2012) examined reflectivity observations across many storms from the Tropical Rainfall Measuring Mission Precipitation Radar and found that outer rainband convection had higher altitude reflectivity peaks than those of inner rainband convection, consistent with the current updraft observations. Previous modeling studies also showed that outer rainbands had greater quantities of convective updrafts (Li and Wang, 2012a; Li et al., 2017).

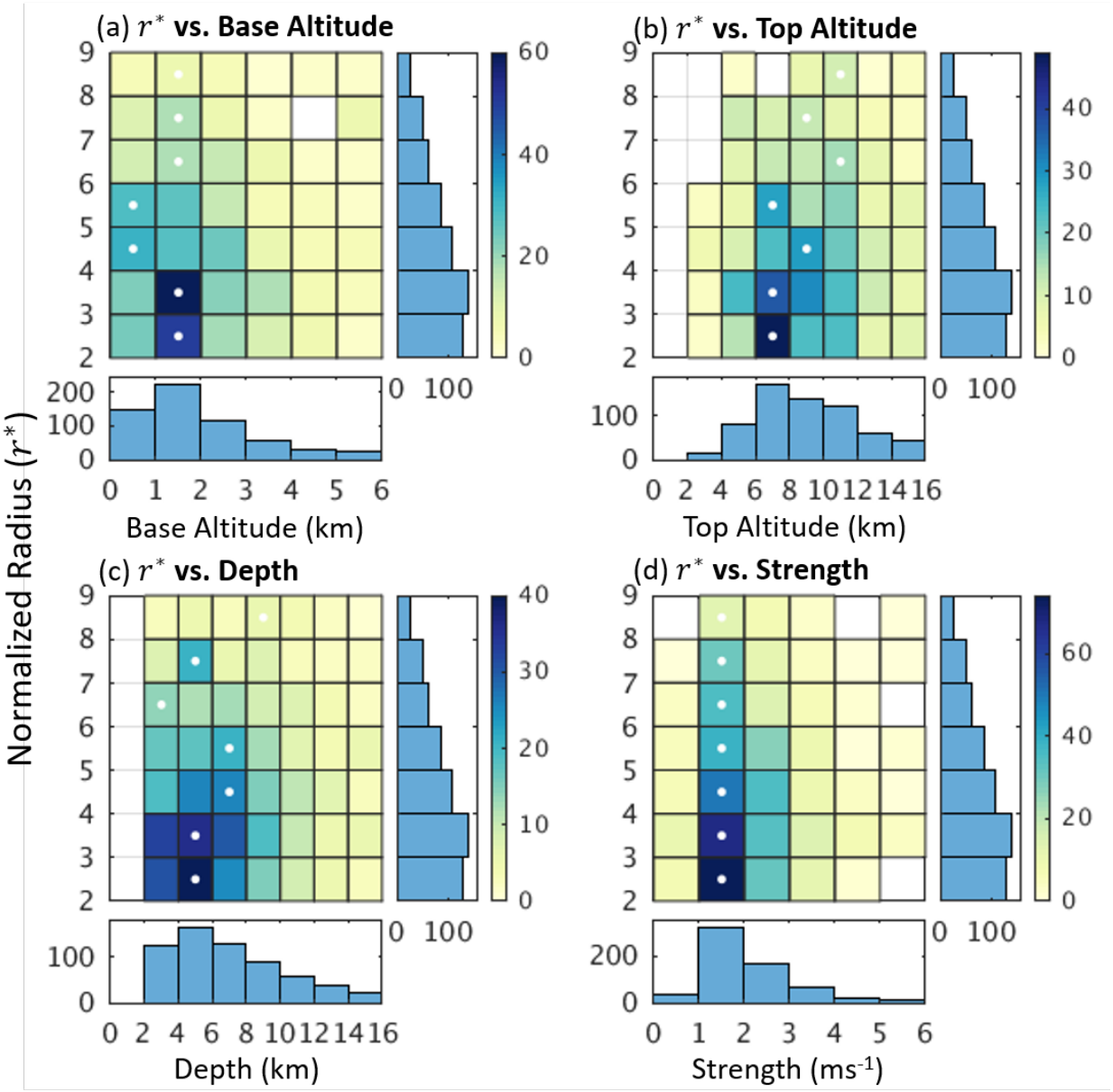

Figure 3.1. Bivariate histograms of updraft normalized radius (r^*) vs. (a) updraft base altitude, (b) updraft top altitude, (c) updraft depth, and (d) updraft strength. Along each axis are the single-dimension histograms for each variable. Frequency counts are shown by the colorbar. White dots indicate the mode of the distribution within each ordinate bin.

Chapter 4
Updraft size, strength, and location in an asymmetric framework

We now analyze the updraft frequencies and characteristics with respect to their azimuthal location; this analysis will highlight asymmetric variations in convective rainband patterns. Figure 4.1a shows the joint frequency distribution of updraft normalized radius vs. shear-relative azimuthal angle. The single-dimension shear-relative angle histogram shows that updrafts more frequently occur downshear with a slight tendency towards the downshear-left (DL) quadrant; this finding agrees with previous observations and modeling studies (Li and Wang, 2012b; Hence and Houze, 2012). In the left-of-shear storm half, the modes appear in a pattern that moves radially inward, which may indicate a spiral convective rainband repeated across many storms.

Previous studies have shown that a shear-organized rainband complex generally occurs with moderate or strong ($\geq$ 5 ms^{-1}) environmental shear (e.g., Corbosiero and Molinari 2002; Rogers et al. 2003; Wingo and Cecil 2010; Hence and Houze 2012). To account for this, Fig. 4.1b limits the above updrafts by requiring a shear magnitude of at least 4 ms^{-1} for the observation period. While 5 ms^{-1} has been used as the threshold for weak to moderate shear in many previous studies, we chose to use 4 ms^{-1} instead to include more elements from our dataset; we did not find a notable difference between selecting 4 or 5 ms^{-1} as our threshold that affects our conclusions.

In Fig. 4.1b, the left-of-shear half exhibits the same inward moving modal pattern as in Fig. 4.1a; this updraft spiral is consistently prominent at stronger shear values. One notable difference in Fig. 4.1b is a clearer local maximum in the single-dimension

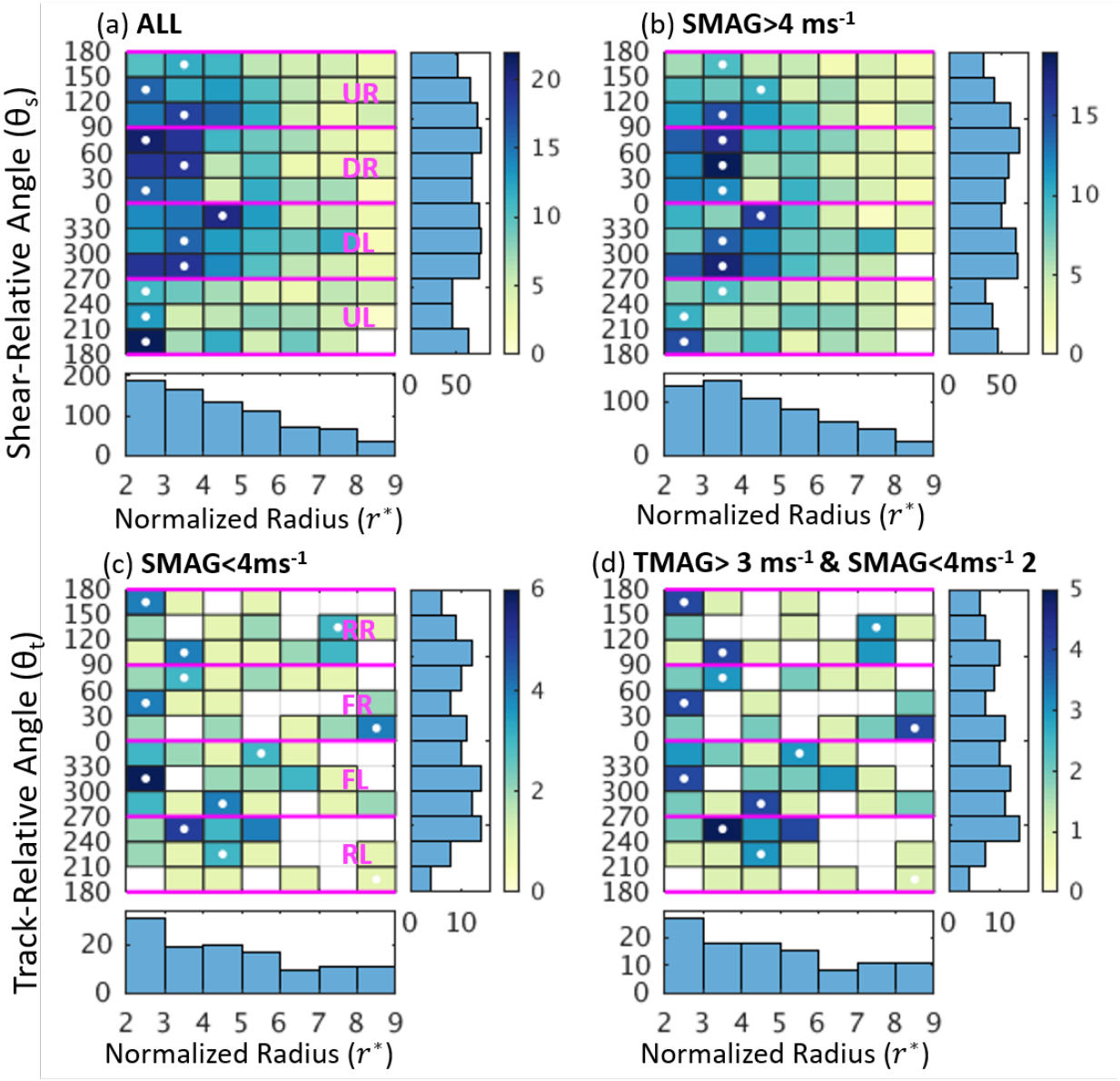

Figure 4.1. Bivariate histograms of (a,b) updraft shear-relative angle (°) vs. r^* and (c,d) updraft track-relative angle (°) vs. r^*. Missions with shear magnitudes (SMAG) > 4 ms^{-1} are in (b). Missions with both storm track magnitudes (TMAG) > 3 ms^{-1} and SMAG < 4 ms^{-1} are in (d). Single dimension histograms and ordinate distribution modes (white dots) are shown. Pink horizontal lines denote the shear-relative quadrants (upshear-right (UR), downshear-right (DR), downshear-left (DL), and upshear-left (UL)) or track-relative quadrants (rear-right, front-right, front-left, rear-left).

updraft frequency between 60-90° in the DR quadrant. Also, the right-of-shear storm half exhibits a steadier mode at 3-4 r^* than that in Fig. 4.1a. Overall, applying the

shear magnitude threshold introduced some additional organization of the frequency pattern, further highlighting the increased rainband convective activity that occurs in a shear-organized Stationary Band Complex (Willoughby et al., 1982; Corbosiero and Molinari, 2002).

In addition to shear, another large-scale influence on rainband azimuthal organization is storm motion, which causes preferential frictional convergence and updraft initiation in the right-of-track quadrants (Corbosiero and Molinari, 2002, 2003). Corbosiero and Molinari (2002, 2003) found that this track-relative organization only occurs when the storm motion is sufficiently fast and the shear magnitude is sufficiently weak. To assess this potential impact, Fig. 4.1c plots the track-relative angle vs. normalized radius for observation periods with a shear magnitude < 4 ms^{-1}, and Fig. 4.1d further restricts this analysis periods with track magnitude > 3 ms^{-1}. Along the single-dimension track-relative histogram, a peak in updrafts occurs in the left-of-track half of the storm. But these updrafts, along with those in the right-of-track quadrants, have varying radii with much less organization when compared to the shear-relative plots. The lack of organization in weak shear cases indicates that the track is not playing a significant role in aligning the rainband convective updrafts in our dataset; albeit, low data counts for weak shear cases may partially explain the disperse signal. Fig. 4.1d appears very similar to Fig. 4.1c, here, indicating that increased track magnitudes further reduce the data count and thus updraft frequencies remain disorganized. Given the importance of shear based on these findings and previous studies, we focus for the rest of this study only on convective updrafts in moderate-to-strong shear (>4 ms^{-1}) cases in order to highlight shear-relative patterns in updraft characteristics.

Azimuthal variations in updraft size and strength variations are also present in the dataset. Figure 4.2 shows these variations with shear-relative azimuth, along with the modes and averages of the distributions. Figure 4.2a shows that the modal base altitude is less than 2 km and the average is ~ 2 km at all azimuths. This average base reaches its highest value (2.3 km) immediately downshear (330-0°), which will be a pertinent finding for later discussions. Meanwhile, the updraft top altitudes (Fig. 4.2b) show scattered modal values at all azimuths. But, the mean updraft top remains close to 9 km throughout the downshear quadrants (270-0°, 0-90°), while upshear, the mean updraft has lower tops, with a minimum occurring at 180-210° of ~ 7.8 km. The distribution of updraft depths (Fig. 4.2c) is wider in the downshear-right (DR) and DL quadrants compared to those distributions upshear. While the modes do not change greatly from upshear to

downshear, slightly deeper averages are occurring downshear. In Fig. 4.2d, the modal strength remains steady at 1-2 ms^{-1}. There is a slightly wider distribution in the DL, otherwise all other quadrants demostrate a similarly shaped distribution. Directly upshear (150-210°), the average strength appears greatest, but this increase may be the result of a smaller sample size. On the whole, convective updrafts more frequently occur in the downshear storm half, and these updrafts have greater depths and have higher tops than those upshear.

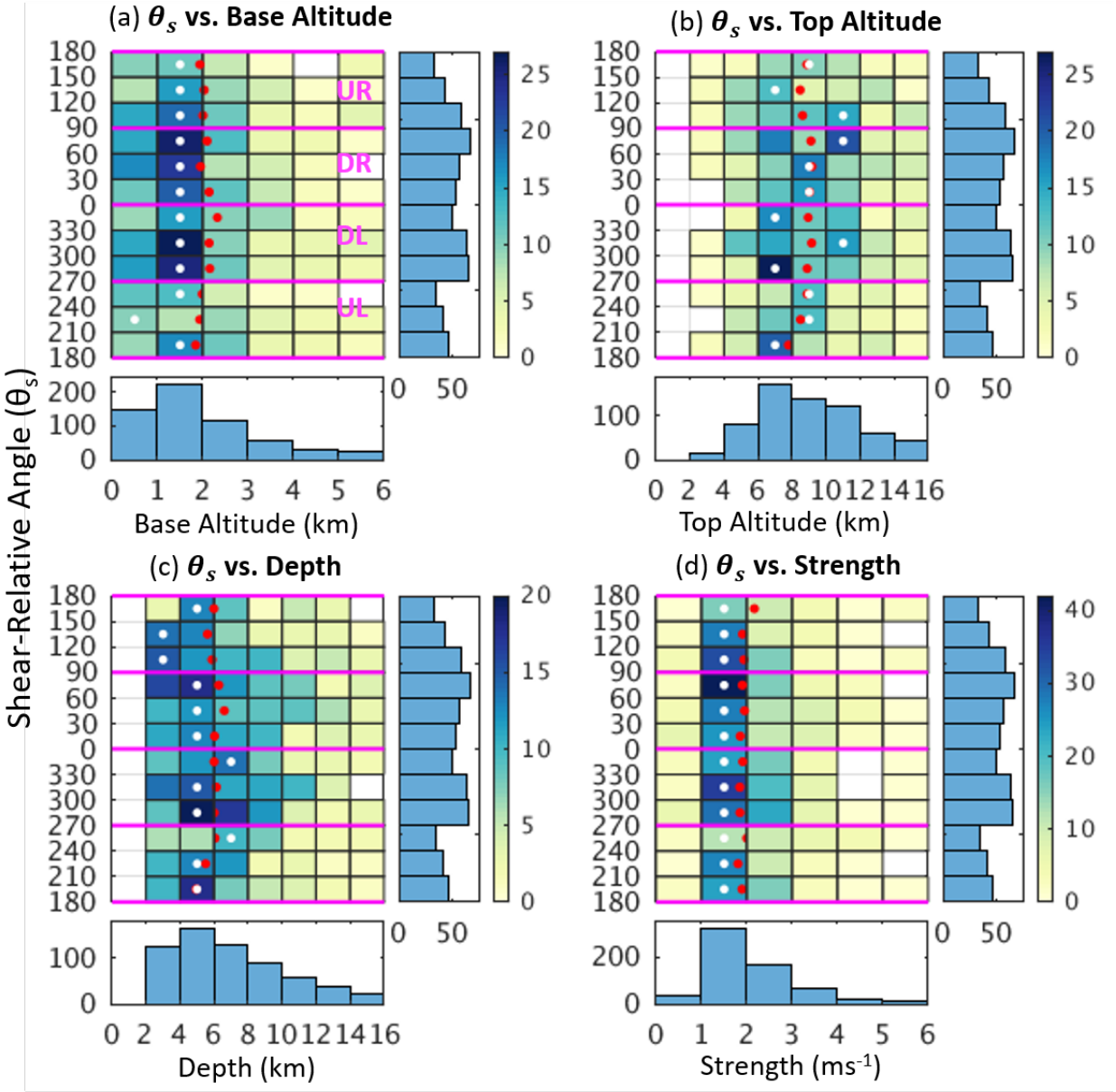

Figure 4.2. As in Fig. 3.1, but for updraft shear-relative angle (°) vs. (a) updraft base altitude, (b) updraft top altitude, (c) updraft depth, and (d) updraft strength. White and red dots indicate the mode and mean, respectively, of the distribution within each ordinate bin.

Chapter 5
Total kinematics of updraft elements

5.1 Quadrant-averaged composites

The previous statistics show the variety of different rainband updraft characteristics across several storms. In order to better understand the processes associated with these updrafts, we need to examine their full convective kinematic structures. We now examine kinematic composites of updraft elements within each shear-relative quadrant. These composites are formed by using the vertical-velocity-weighted centroid for each updraft as an anchor to cut a radial cross-section of the velocity and reflectivity fields. Tangential wind perturbations are calculated by subtracting from each point a moving, azimuthal average that spans ±45° from the anchored azimuthal coordinate. In this manner, wavenumber-1 and -2 asymmetries in tangential velocity are removed. Figure 5.1 shows updraft-centered composites of radial and vertical velocity, tangential velocity perturbation, and reflectivity for each shear-relative quadrant.

Each quadrant composite shows a unique radial and vertical circulation pattern. First, an in-up-out signature is present in the downshear quadrants (Figs. 5.1a,b), and an out-up-out signature in the upshear quadrants (Figs. 5.1c,d). The low-level flow of these convective circulations matches that of the radial velocity wavenumber-1 asymmetry expected for TCs experiencing environmental wind shear (Jones, 1995; Bender, 1997; Reasor et al., 2004). A sheared vortex tends to develop a vertical tilt that is pointed in the downshear direction. As a result, the vortex generates a balanced secondary circulation response of enhanced low-level radial inflow downshear and enhanced low-level outflow

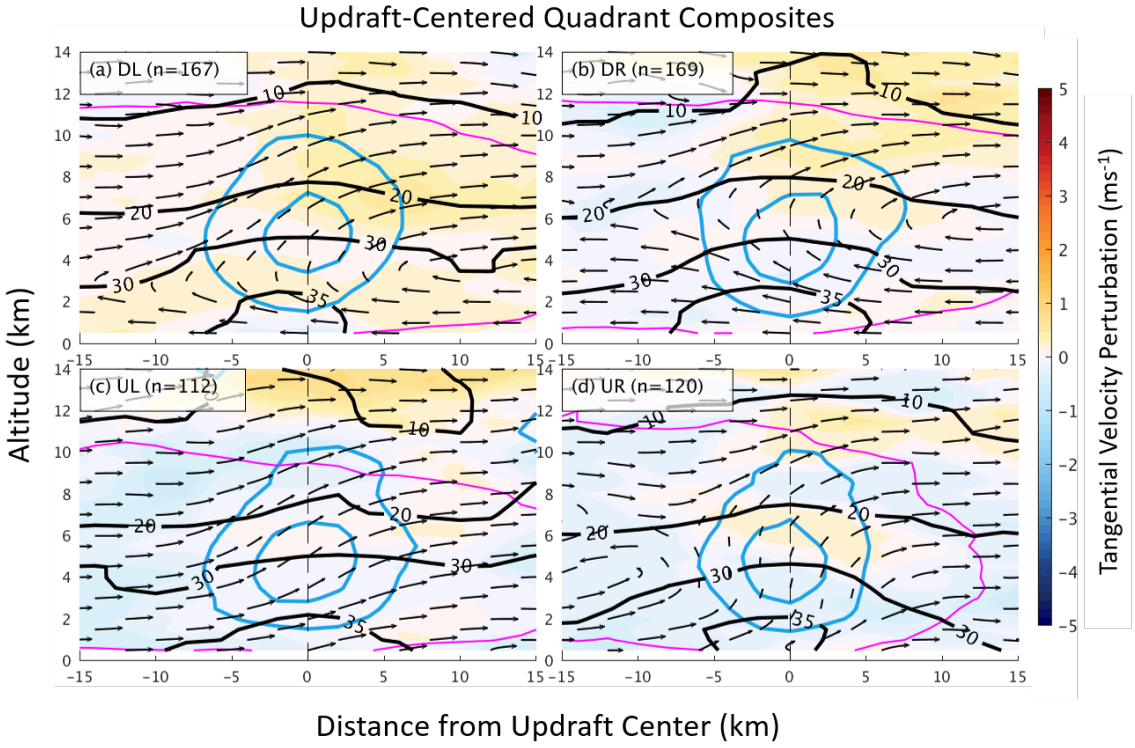

Figure 5.1. Composite radial cross sections of updrafts in each shear-relative quadrant: (a) DL, (b) DR, (c) UL, and (d) UR. Composites are radially centered on the updraft centroid. Normalized vertical velocity contours are drawn in blue at intervals of 0.5 and 1, where velocities are normalized by the updraft threshold for each mission. The flow along the radial and vertical direction is shown as streamline vectors. Tangential velocity perturbations are shown as shaded contours. Reflectivity contours are drawn in black at 10, 20, 30, and 35 dBZ. The magenta contour outlines locations with < 50% of data missing from the cross sections included in the composite. The number of cross sections, n, in each composite is shown.

upshear, extending from the eyewall to the rainband regions of the storm (e.g., Frank and Ritchie 1999, 2001; Zhang et al. 2013). The downshear inflow layer shrinks from ~ 6 km in the DR to ~ 2.5 km in the DL (Fig. 5.1a,b), consistent with findings previously documented from observation composites (Reasor et al. 2013; Rogers et al. 2013). In the upshear-left (UL) quadrant, the outer vertical velocity contour is deeper than that in the downshear quadrants, but this is likely caused by poor representation in the data.

In addition, each shear-relative composite has a clear positive tangential wind perturbation. Its exact location varies, but the perturbations in the upshear-right (UR), DR, and UL are at or above 6 km altitude and overlap the transition of low-level inflow to upper-level outflow. These perturbations are likely the midlevel tangential jet observed in

convective rainbands from previous studies (e.g., Barnes et al. 1983; Hence and Houze 2008). The DL has a broad, deep area of positive tangential wind perturbation. This broad enhancement may be tied to mesoscale features that often occur in the DL region of a shear-aligned rainband complex. Here, convective updrafts can be embedded in a larger, predominantly stratiform rainband that has broad mesoscale uplift, which can produce broad, deep acceleration of the tangential wind (Didlake and Houze, 2013b).

5.2 Classification of updraft circulation patterns

The quadrant composites provided a first look at the dominant convective updraft circulation patterns throughout a TC, but circulation variations within each quadrant may be obscured by the composite averaging. To better capture the varying characteristics of the radial/vertical velocity circulations, we derive an objective classification scheme that delineates common circulation patterns associated with rainband convective updrafts. Four idealized circulations are identified and illustrated in Figure 5.2. The four circulation types are defined as (1) in-up-in, (2) out-up-out, (3) in-up-out, and (4) out-up-in (Fig. 5.2a-d).

To quantitatively define each circulation, four measurements are taken of the kinematics at and around the updraft. First, a radial cross section is taken through the updraft centroid. In this cross section, two boxes are drawn that bisect the updraft in the vertical direction at its centroid and extend out ±10 km in the radial direction (Fig. 5.2e-h). Radial velocity and azimuthal vorticity are then calculated for each point and averaged over the domain of each box, resulting in four deterministic measurements: top velocity, top vorticity, bottom velocity, and bottom vorticity. Different combinations of each measurement across the two boxes ideally describe the four circulation types (as shown in Fig. 5.2a-d). However, rather than using strict Boolean expectation ranges for each classification, we use a probabilistic method to allow a small amount of flexibility within each expected measurement range, which leads to a better overall scheme.

We define an arbitrary probability density kernel (PDK) for each expectation value, Y_{ji} (shown in Table 5.1), where j and i are the circulation type and measurement indices, respectively. The measured value (X_i), either velocity or vorticity, is then used to assign a sub-probability p_{ji}, calculated from the PDK function of a Gaussian distribution, given

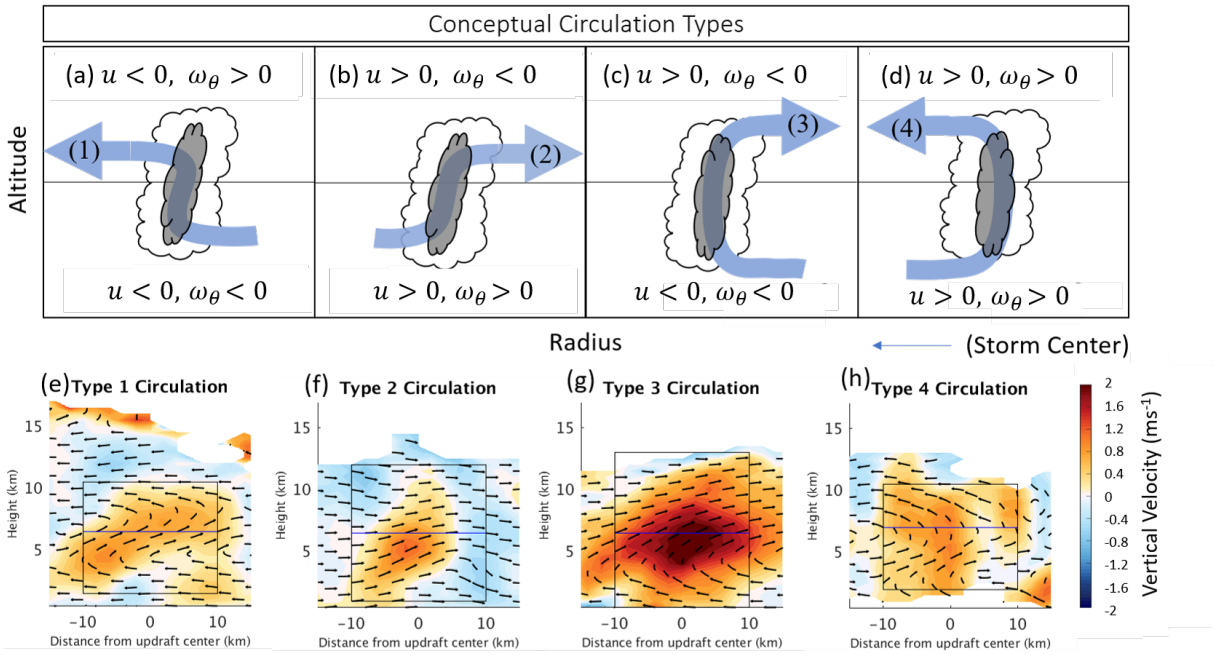

Figure 5.2. (a-d) Schematic of the four circulation types as defined by the circulation classification algorithm for rainband convective updrafts. Updrafts are sketched in gray and embedded in an outlined cloud. Idealized streamlines in the $r-$z plane for each circulation type are shown in light blue. The expected signs for the azimuthal vorticity (ω_θ) and radial velocity (u) are indicated in the upper and lower boxes. (e-h) Example convective updraft cross sections for each classification type. Streamline vectors depict the radial and vertical flow. Filled contours show the vertical velocity. Upper and lower boxes are divided at the updraft centroid and bounded by top and base altitudes and ±10 km from the updraft center.

Table 5.1. Table of the expectation value (Y_{ji}) for each of the four measured quantities (X_i) and classification types used for the circulation type algorithm. The indices j and i represent the circulation type and measurement indices, respectively.

Measurement	Expectation (Y_{1i})	Expectation (Y_{2i})	Expectation (Y_{3i})	Expectation (Y_{4i})
Top Radial Velocity (X_1)	$Y_{11} < 0$	$Y_{21} > 0$	$Y_{31} > 0$	$Y_{41} < 0$
Top Azimuthal Vorticity (X_2)	$Y_{12} > 0$	$Y_{22} < 0$	$Y_{32} < 0$	$Y_{42} > 0$
Bottom Radial Velocity (X_3)	$Y_{13} < 0$	$Y_{23} > 0$	$Y_{33} < 0$	$Y_{43} > 0$
Bottom Azimuthal Vorticity (X_4)	$Y_{14} < 0$	$Y_{24} > 0$	$Y_{34} < 0$	$Y_{11} > 0$

by

$$p_{ji} = \begin{cases} \frac{1}{b\sqrt{2\pi}} \int_{-\infty}^{X_i} e^{-(\frac{x-a}{4b})^2} dx & \text{for } Y_{ji} < 0 \\ \frac{1}{b\sqrt{2\pi}} \int_{X_i}^{\infty} e^{-(\frac{x+a}{4b})^2} dx & \text{for } Y_{ji} > 0 \end{cases}, \tag{5.1}$$

where a and b are Gaussian distribution parameters (the mean and standard deviation, respectively). The values of a and b are chosen to be equal to 1; this choice ensures that

calculations do not produce rounding errors in the following procedures.

The sub-probability acts as a weight, ranging between 0 and 1. For a given cross section, p_{ji} is calculated for each combination of the four measurements and classifications. The products of the sub-probabilities for each measurement expectation is calculated for each potential type, given by

$$P_j = p_{j1} \times p_{j2} \times p_{j3} \times p_{j4}. \tag{5.2}$$

Of the four values of P_j, the greatest value, $P_{j_{\max}}$, determines the circulation type, assigned as $j_{\max}$ for a given cross section. By using this method, the classification scheme can forgive a single measurement for a classification type that is not matching the sign of the expectation value and still punish the classification types that are not appropriate for that updraft cross section. This methodology was tested by analyzing the cross section velocity fields and subjectively assigned a classification type, then by comparing this qualitative analysis to the quantitative algorithm defined above; the two methods compared very well. Figs. 5.2e-h show example cross sections for each classification type.

5.3 Updraft characteristics for each circulation type

Figure 5.3 shows the joint frequency plots of location, size, and strength vs. the circulation classification types. As seen in the single-dimension type frequency counts, type 2 (out-up-out) and 3 (in-up-out) circulation types are most frequent. Type 1 (in-up-in) circulations are still frequent, but not so much as the type 2 and 3 updrafts. Although type 4 (out-up-in) circulations are possible, particularly in the upshear quadrants (Fig. 5.3a), the frequency counts are quite low comparatively, and thus, type 4 will not be considered further in this analysis.

Starting at $\theta_s = 180°$ in Fig. 5.3a, type 2 (out-up-out) is sustained for most of the UR ($180° < \theta_s < 120°$). Moving downwind, the more frequent circulations shift to types 1 (in-up-in) or 3 (in-up-out) for $120° > \theta_s > 0°$, covering the entire DR quadrant. Continuing further downwind, the DL quadrant consists of high frequencies of all three circulation types, with a notable increase in type 2. The overall frequency signal changes to primarily type 2 in the UL quadrant. The observed pattern of circulation type frequencies generally follows the expected low-level radial flow of a sheared storm (Jones, 1995; Bender, 1997).

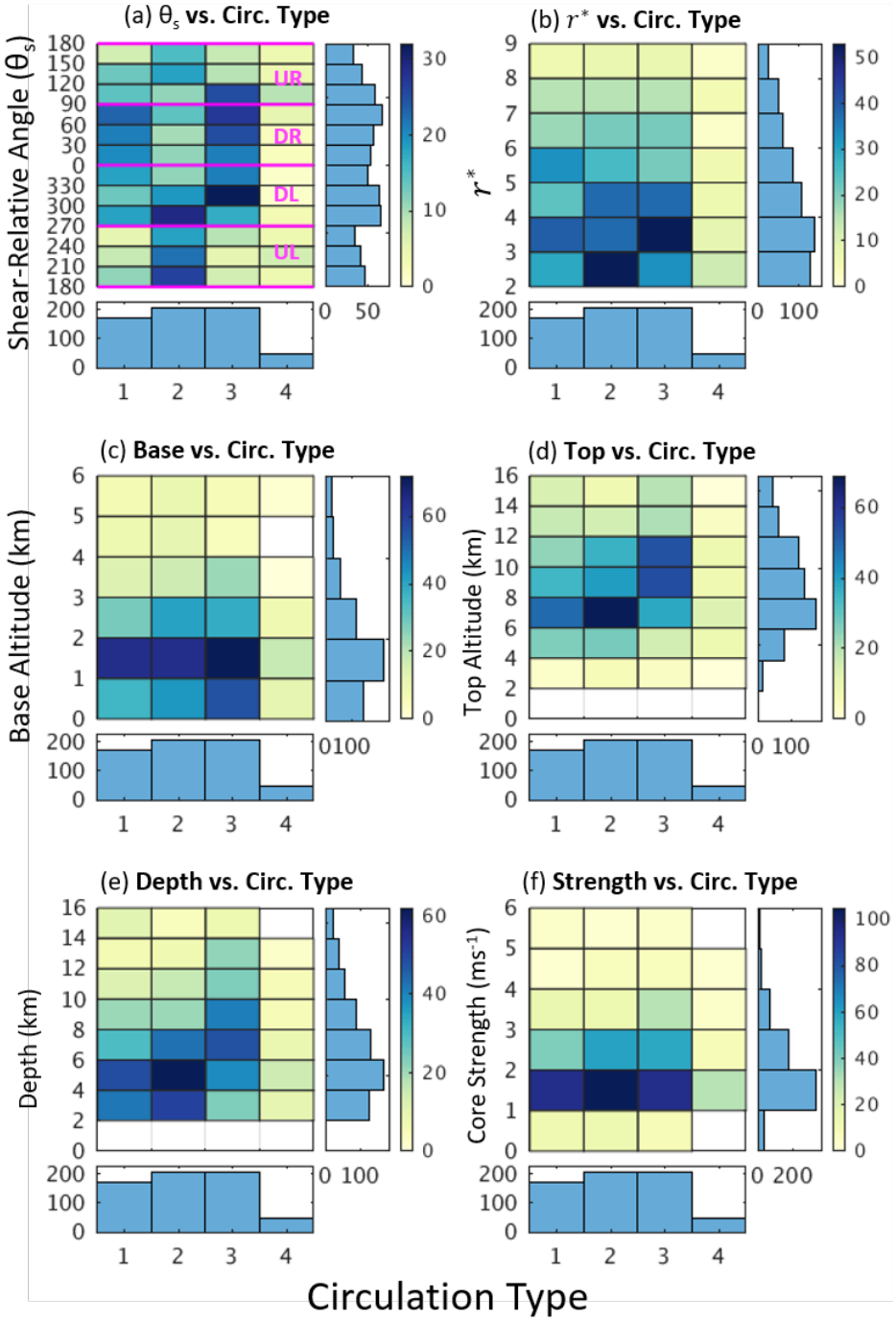

Figure 5.3. As in Figs. 3.1 and 4.1 but for circulation classification type vs. (a) shear-relative angle (°), (b) normalized radius (r^*), (c) updraft base, (d) updraft top, (e) updraft depth, and (f) strength.

In the upshear quadrants, low-level outflow corresponds to a type 2 or type 4 circulation, and in the downshear quadrants, low-level inflow corresponds to a type 1 or 3 circulation. Still, notable exceptions are present, such as the frequent occurrence of types 1 and 3 in the UR and type 2 in the DL.

Figure 5.3b shows the normalized radius vs. updraft circulation type. Here, type 1 circulation has a broad distribution covering most radii, with two frequency peaks occurring at 3-4r^* and 5-6r^*. Type 2 updrafts tend to occur at smaller radii with a mode at 2-3r^* and have reduced frequencies beyond 5r^*. Type 3 circulation has a narrower distribution with a mode between 3-4r^*. Figures 5.3c-e show the frequencies of updraft base altitude, top altitude, depth, and strength for each circulation type. The dominant updraft characteristics are generally consistent across types 1 and 2, while type 3 shows some deviations. Most updraft bases are between 1-2 km, while type 3 has a higher tendency of bases between 0-1 km than other types (Fig. 5.3c). Most updrafts for all types do not have bases higher than 3 km. Types 1 and 2 have updraft tops most often between 6 and 8 km, while type 3 tops are most frequent at higher altitudes, often reaching 8-12 km (Fig. 5.3d). Fig. 5.3e shows that, in general, types 1 and 2 updrafts are between 2-8 km deep, while type 3 updrafts are clearly the deepest, spanning depths of 4-14 km. Updraft strength (Fig. 5.3f) does not vary much with circulation type, largely remaining between 1-2 ms^{-1}. However, the distribution tails indicate that type 3 updrafts are the strongest. In summary, type 3 updrafts have lower bases, higher tops, deeper extents, and stronger magnitudes than the other types.

While the low-level radial flow direction of updraft circulations generally corresponds to the vortex-scale radial flow, this analysis also shows that the midlevel radial flow direction is possibly tied to the updraft depth and midlevel tangential jet. Deeper updrafts are more likely to generate a midlevel tangential jet, which, through conservation of angular momentum, ejects the flow radially outward and presents as either type 2 or 3 circulations. Shallower updrafts are less likely to generate a jet, and thus continue radially inward as in the type 1 circulation.

Our defined circulation types have been identified in several past studies. The deep and frequent type 3 (in-up-out) updraft is the same as that studied in several observation studies (Barnes et al., 1983; Barnes and Stossmeister, 1986; Powell, 1990a,b; Barnes and Powell, 1995; Samsury and Zipser, 1995; May, 1996; Hence and Houze, 2008; Didlake and Houze, 2009, 2013b; Tang et al., 2018; Yu et al., 2018) and modeling studies (Li and Wang, 2012a; Moon and Nolan, 2015). These prominent features were generally found

in the principal rainband of the organized rainband complex, and often exhibited deep radial inflow like these examined in the current study. Type 1 (in-up-in) updrafts tended to be observed in distant outer rainbands that propagated radially outward like squall lines (Barnes et al., 1991; Ryan et al., 1992; Yu and Tsai, 2013; Moon and Nolan, 2015; Yu et al., 2018). Their kinematic and thermodynamic structures also indicated that squall line dynamics governed the evolution of the rainband evolution. Moon and Nolan (2015) showed that simulated inner rainbands can also exhibit type 1 updrafts (see their Fig. 15), but these updrafts were quite short, reaching only up to 4 km altitude. Tang et al. (2014) studied convective cells within the principal rainband (located at intermediate radii) and found similar circulations to types 1 and 3; they also noted that the type 3 circulations led to taller cells. Type 2 circulations were found in Didlake and Houze (2013b) and Didlake et al. (2018). Didlake and Houze (2013b) showed updrafts with an elevated base ($\sim$ 3 km) and shallow depths ($\sim$ 4 km), while Didlake et al. (2018) showed rainband updrafts with a 0.5 km base and 13 km depth.

5.4 Azimuthal variations in updraft size, location, and circulation type

Azimuthal variations in updraft characteristics were first noted in the distributions and averages of Fig. 4.2. These variations become more pronounced when examined by circulation types. Figure 5.4 plots averages of the updraft base altitude, top altitude, and depth against the shear-relative angle and separated by circulation type. These averages, starting from the UR to the UL, provide a snapshot of how the aggregate of updrafts are evolving as they propagate around the storm. Also shown are confidence intervals at the 95% level (calculated using a two-sided Student's t-test) to determine the statistical significance of the differences between each average.

Type 1 updrafts (Fig. 5.4a) have base altitudes that range from ~3.5 km in the UR to 2 km in the DR, and back up to ~4 km in the UL. Going from UR to DL, the average depth grows from 5.5 km to 6.5 km and the average top grows from 8 to ~10 km. In the UL quadrant, these values decline, but the number of sampled updrafts is very low, which suggests that the average here may not be wholly representative.

Type 2 updrafts (Fig. 5.4b) exhibit a different pattern, with a minimum base altitude of 2.5 km in the UR, then increasing to a maximum of 4 km altitude in the DR and DL.

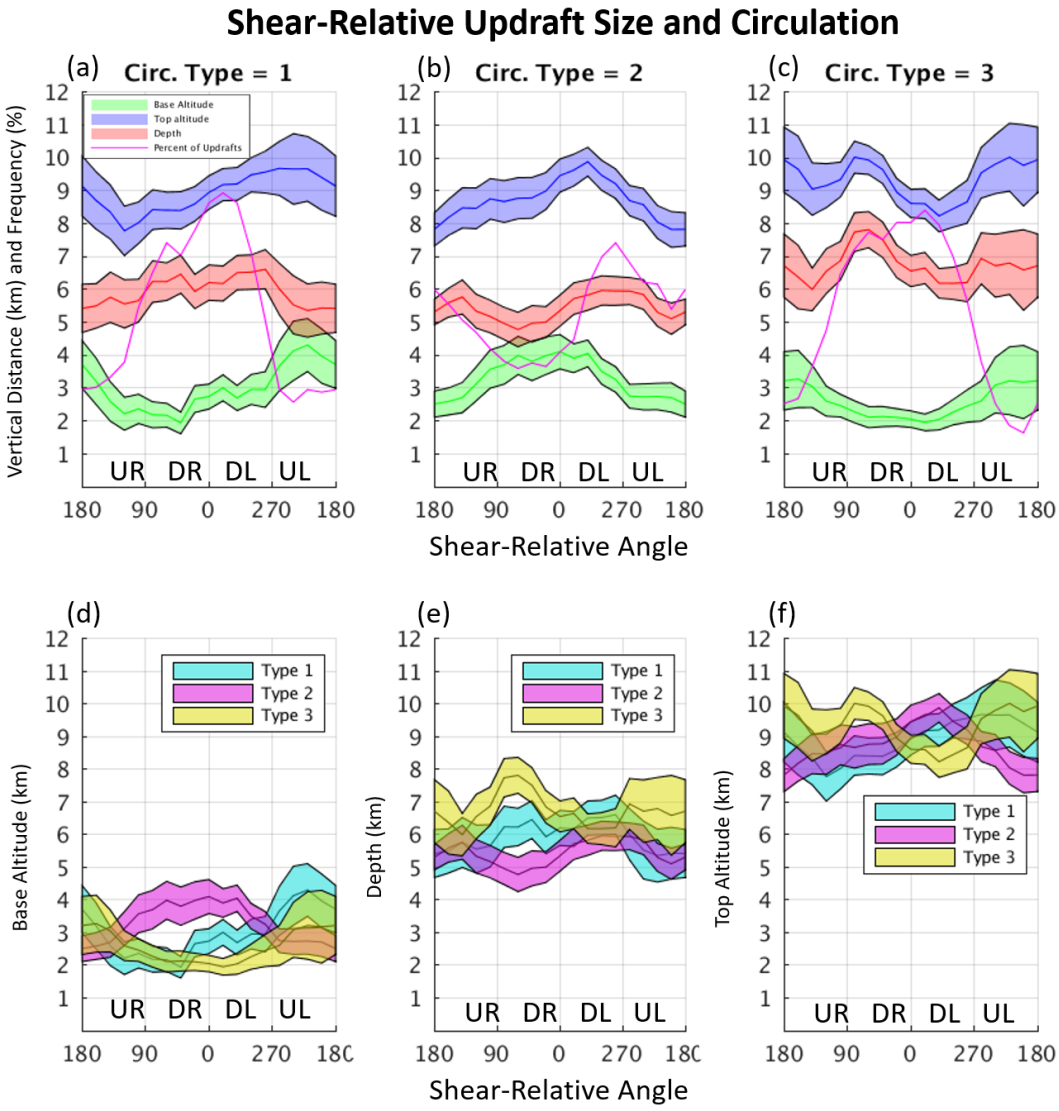

Figure 5.4. (a-c) Average values of updraft base altitude, depth, and top altitude as a function of shear-relative angle (°) stratified by circulation type. Values are calculated every 20° in a moving azimuthal average over ±30°. Shaded regions represent the statistical significance confidence intervals at the 95% level. The frequency of updrafts is shown in magenta as the percent of total updrafts at each azimuth. Shear-relative quadrants are labeled at the bottom moving cyclonically from left to right. (d-f) Same as (a-c) but stratified by updraft base, depth, and top.

The type 2 base altitude of 4 km is statistically significantly higher than the base altitudes of types 1 and 3 in these same quadrants (Fig. 5.4d). The number of type 2 updrafts jumps appreciably going from downshear (0°) to the end of the DL quadrant. In the DL

quadrant, the type 2 average top altitude reaches its peak of 10 km, which is statistically significantly higher than type 3 (Fig. 5.4f).

Type 3 updrafts (Fig. 5.4c) exhibit yet another pattern, beginning with an average base altitude between 2-3 km and reaching its minimum in the downshear quadrants. The distributions in Fig. 5.3 indicated that type 3 updrafts are generally deeper and taller than both types 1 and 2. Figs. 5.4e-f show that this type 3 difference is statistically significant in the DR quadrant (90-30°), reaching 8 km deep and 10 km top altitude. Both the depths and top altitudes experience a statistically significant decrease from the DR to DL (Fig. 5.4c). Interestingly, this notable decrease coincides with the increase in type 2 frequency, depth, and top height, indicating an opposite behavior of evolving type 2 and 3 characteristics. As with type 1, type 3 in the UL quadrant suffers from low sample size, so the average is likely not representative of the updrafts occurring in that area.

The updraft characteristics and circulation patterns described herein may be the manifestation of the convective life cycle as updrafts propagate downwind within an organized rainband complex. Rainband convection begins to form in the UR as denoted by the increase in updraft frequency between 150-70° in both types 1 and 3. Although present, type 2 decreases in frequency likely due to the changing vortex-scale low-level inflow entering the downshear quadrants. As these updrafts travel downwind, they intensify, as shown by the greater depths in the UR to DR for types 1 and 3. Similar findings are presented by Li and Fang (2019) in their study of convection and buoyancy, with the convection that is directly downshear experiencing more buoyancy. Then, as the convection ages and travels further downwind, prominent stratiform precipitation begins to form early in the DL quadrant (see Hence and Houze 2012; Didlake and Houze 2013b). The opposite behavior of the type 2 and 3 frequency and depth occurs here, and is possibly caused by a transition in updraft circulations going from type 3 to type 2. During this transition, strong in-up-out (type 3) circulations are cut off in the lower levels by a combination of a shrinking low-level inflow layer and increased low-level downdrafts from evaporation within the growing stratiform precipitation. For an updraft population being advected downwind, a shrinking vortex-scale inflow layer would result in increasing type 2 frequencies at the expense of type 3 frequencies, given that a steady updraft base would gradually be removed from the low-level inflow layer. Additionally, these type 2 updrafts downwind would have a lower base altitude than those at upwind azimuths. At the same time, type 2 base altitudes remain higher than those of type 3 throughout the DL quadrant (Fig. 5.4d). As this quadrant generally is where many convective cells

begin to collapse, low-level downdrafts from evaporation become more prevalent. These downdrafts would in turn erode away the updraft base of type 3 updrafts, elevate the cloud base to above the inflow layer, and turn them into type 2 updrafts.

Still, going further downwind from DL to UL, type 2 circulations show a decrease in base altitude, indicating a process shift that lowered the altitude of convective updraft triggering. This pattern is consistent with an increased role of stratiform precipitation dynamics in this region where surrounding stratiform precipitation continues to increase in prominence (Didlake and Houze, 2013b; Yu and Didlake, 2019). The increased low-level evaporation and latent cooling within the dominant stratiform region introduces a broad cold pool that sinks and interacts with the boundary layer. The result is the initiation of new convection by creating an area of low-level convergence as the inflow layer interacts with the evaporation-driven cold pool (Yu and Didlake, 2019). More specifically, low-level updrafts can be caused by azimuthal buoyancy advection across the low-level temperature gradient created by the stratiform precipitation. The resulting circulation would be more like type 2 given that the background radial inflow layer is shallower in this region of the storm. These dynamics and resulting circulations were also observed in Didlake and Houze (2013b) and Didlake et al. (2018).

In order to focus further on the updraft types presented previously, a carefully selected composite approach is used. Figure 5.5 shows composite cross sections of specific azimuthal and radial ranges, similar to Fig. 5.1 but separated by the circulation type. Figure 5.5a is the same as Fig. 4.1b, showing all updraft frequencies by shear-relative azimuth vs. normalized radius, but now with regions highlighted by boxes. Figures 5.5b-d present the corresponding composite cross sections for the chosen boxes. These box regions were specifically selected to further illustrate details of the updraft characteristics described previously. This behavior is similar to that found in Fig. 5.1. The UR-DR region (Fig. 5.5b) shows a joint in-up-in/in-up-out circulation with the outer vertical velocity contours spanning $1-8.5$ km altitudes. A deep inflow layer is present here with a switch to outflow occurring around 5 km altitude. In the DR-DL region (Fig. 5.5c), all reflectivity contours are deeper, along with a bell-shaped 30 dBZ reflectivity contour. The in-up-out circulation is dominant and the inflow layer is slightly shallower than in Fig. 5.5b. The DL-UL composite in Fig. 5.5c shows different features from the upwind panels. The circulation has a shallow inflow region that turns outward at about 2.5 km, similar to Fig. 5.1a. But, unlike in Figs. 5.5b and c, there is no clear reflectivity tower, and the reflectivity contours are nearly horizontal, indicating an increasing amount of

stratiform precipitation surrounding the convective updraft.

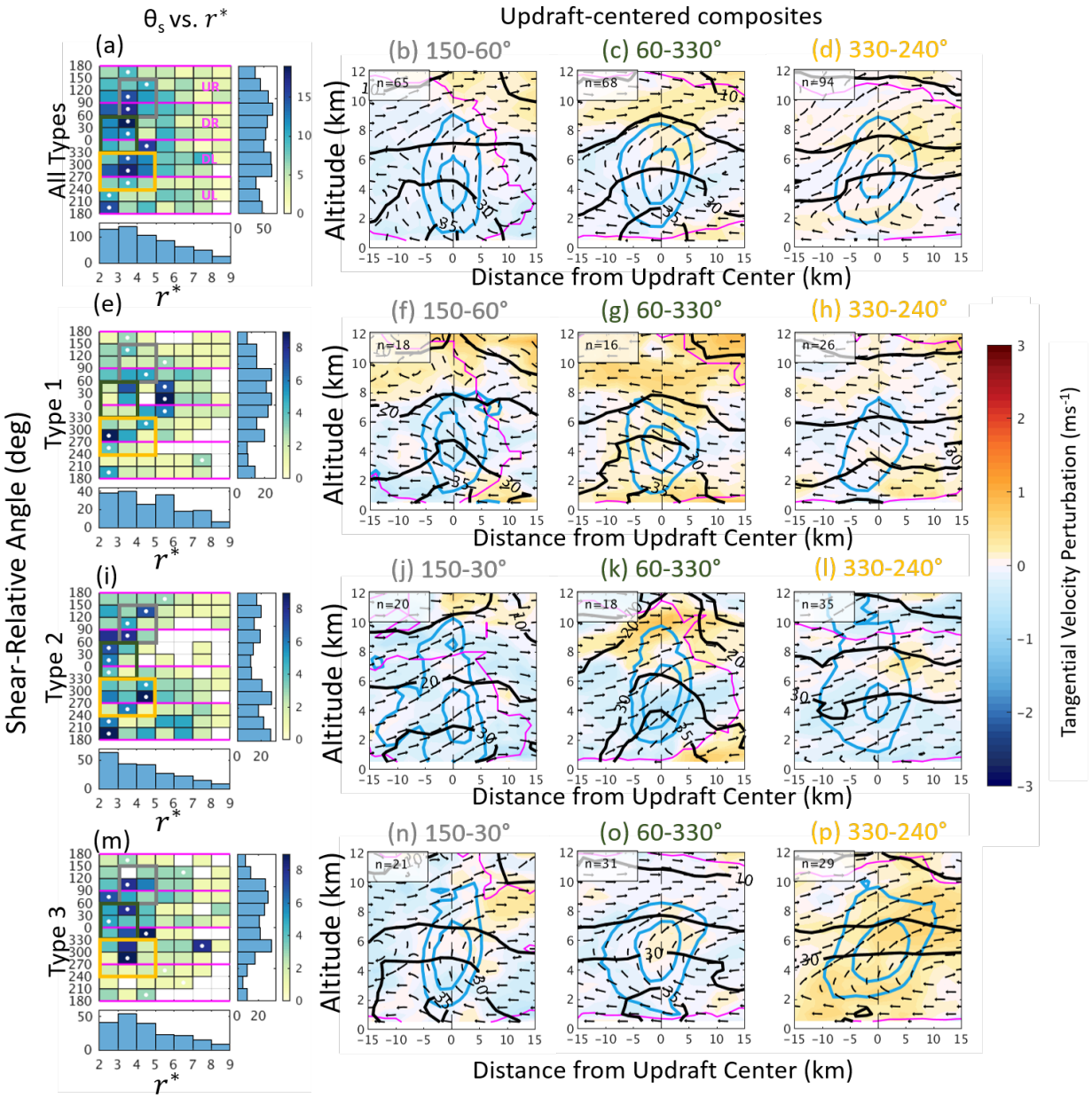

Figure 5.5. As in Figs. 4.1 and 5.1 but stratified by circulation type: (a-d) All types 1-4, (e-h) type 1, (i-l) type 2, and (m-p) type 3. The first column (a,e,i,m) shows the joint frequency histogram of shear-relative angle (°) vs. r^* for the corresponding updrafts. The following three columns are cross section composites using only updrafts within the radial and azimuthal ranges denoted by the colored boxes in the first column. Above each composite are the corresponding azimuthal ranges and box colors. The number of updrafts used in the composite average, n, is shown.

Figures 5.5e-h feature only type 1 updrafts. Figure 5.5e shows a broad radial distribution of type 1 updrafts consistent with Fig. 5.3b. The cross sections from our select boxes show that type 1 reflectivity contours follow the same trends shown in the overall average in Fig. 5.5b-d. The updrafts are consistently less deep with weak vertical velocities when compared to the total average. In particular, type 1 updrafts are weaker and shallower (smaller depth and top) than type 3 (Figs. 5.5n-p), consistent with Figs. 5.3 and 5.4.

Type 2 updrafts are mostly present in two distinct bands (right-of-shear and left-of-shear) that are both captured by the box regions (Fig. 5.5i). The type 2 composites show some of the most variable behavior across the series. In the UR-DR region (Fig. 5.5j), a wide swath of the outer vertical velocity contour is shown, but the exact shape of this contour may be impacted by the lack of data representation (note the 50% data contour). However, the relatively small size of the inner contour indicates that these updrafts are not particularly strong. Just downwind, the next composite (Fig. 5.5k) shows a more cohesive updraft with a larger inner contour. In the DL-UL region, Fig. 5.5l displays a taller, wider, and weaker updraft. The reflectivity measurements show a horizontal 30 dBZ contour that suggests surrounding widespread stratiform precipitation. The distinct differences in both appearance (i.e. changing from tightly packed vertical velocity contours and bell-shaped reflectivity contours to more spaced vertical velocity contours and horizontal reflectivity contours; Figs. 5.5k-j) and radial position (Fig. 5.5f) going from DR to DL suggest that these type 2 updrafts are from different populations with different dynamical origins. This hypothesis would also account for the sharp increase in size and frequency that was observed in Fig. 5.4.

Type 3 updrafts (Fig. 5.5m-p) are generally the most intense updrafts when compared with the total average, type 1, and type 2 box composites, consistent with previous analyses in Figs. 5.3 and 5.4. This is demonstrated by a relatively intense vertical velocity structure in each composite and a correspondingly large inner vertical velocity contour.

Figure 5.4 highlighted the opposing shifts in updraft characteristics and frequency between types 3 and 2 in the DR-DL regions, which led to the hypothesis that type 3 transitions to type 2. This shift is further emphasized by the location-dependent transition in frequencies found in Figs. 5.5i and 5.5m. As the frequency of type 3 updrafts diminishes at 3-5r^* and 0-270°, the frequency of type 2 updrafts increases; the radial and azimuthal positions of these frequency changes exactly match, which further supports the idea that such a transition occurs. As described earlier, this type-3-to-type-2 transition

is likely a result of the inflow layer decreasing below the updraft base and/or low-level downdrafts elevating the updraft base above the background inflow layer. Additional support for increasing type 2 updraft frequencies would be due to the surrounding precipitation becoming increasingly stratiform in nature, wherein a mesoscale cold pool further forces new updrafts that appear in the form of type 2.

Chapter 6
Conclusions

This study examines the kinematic and reflectivity characteristics of rainband convective updrafts observed by airborne Doppler radar across 10 years of Atlantic and east Pacific basin tropical cyclones. Using an objective updraft clustering algorithm, statistics were recorded from each updraft that include measurements of the updraft size, strength, convective-scale secondary circulation, radial location, and azimuthal location relative to the environmental 200-850 hPa wind shear vector. These statistics were analyzed to determine the variety of convective updrafts present in a variety of storms.

On average, convective rainband updrafts become deeper and stronger with increasing radius, likely due to increasing CAPE with radius (Bogner et al., 2000). When analyzed with respect to the wind shear vector, a wavenumber-1 asymmetry in updraft frequency appears, with updrafts being more frequent and deeper in the downshear quadrants of the storm and less frequent and shallower in the upshear quadrants of the storm. This asymmetry aligns closely in structure and orientation with a typical shear-organized rainband complex (Willoughby et al., 1984; Hence and Houze, 2012). Low-level radial flows near the updrafts tend to follow the background vortex-scale radial flow profile, which has a wavenumber-1 asymmetry of increased low-level inflow in the downshear quadrants of the storm and increased low-level outflow in the upshear quadrants. This asymmetry appears as a low-level inflow layer of varying depths; in particular, the downshear inflow layer decreases in depth traveling from the downshear-right to downshear-left quadrants, consistent with previous studies (Jones, 1995; Bender, 1997; Reasor et al., 2013; Zhang et al., 2013).

Figure 6.1 summarizes these findings and additional details in a conceptual model. The plan view reflectivity outlines an organized rainband complex typically seen in a mature, sheared tropical cyclone. In the right-of-shear storm half, the rainband complex

exhibits isolated or connected convective cells that are initiated upwind, then mature and aggregate traveling downwind. Eventually, the cells begin to collapse and transition to stratiform precipitation, which then becomes the dominant precipitation regime in the left-of-shear portion of the rainband complex.

We then analyzed the variation of the observed secondary circulations (radial and vertical velocity) associated with the convective updrafts. To do this, we implemented a kinematic classification system that sorts the flow patterns into four types: (1) in-up-in, (2) out-up-out, (3) in-up-out, (4) out-up-in. The frequencies, distributions, and structures of these circulation types revealed additional context of the typical rainband convective updrafts. Figure 6.1 shows cross sections through downshear updrafts at different shear-relative azimuths, illustrating the overall prominent types of secondary circulations, as well as reflectivity structures, in the most prominent updraft regions. Updraft characteristics in these regions are described as follows:

- UR-DR (Panel I): The frequency of types 1 and 3 updrafts increases cyclonically, and thus they prominently appear. A smaller number of type 2 updrafts do occur, but they have a higher base altitude than types 1 and 3 updrafts. Type 1 updrafts are generally less deep when compared to type 2 or 3 updrafts. Shallow reflectivity towers are present and the inflow layer is about 6 km deep.

- DR (Panel II): The strongest and deepest updrafts occur here, largely types 1 and 3. Deeper updrafts, which produce midlevel tangential wind jets, are more often type 3 circulations given that the accelerated winds are ejected radially outward to conserve angular momentum. Tall, clear reflectively towers and bell-shaped reflectivity contours accompany the convective updrafts. The inflow layer is about 5 km deep.

- Downshear-DL (Panel III): Both types 2 and 3 are prominent, but while the frequency and depth of type 3 decrease throughout this azimuthal region, the frequency and depth of type 2 concurrently increase. This behavior is likely due to the shrinking of the low-level inflow layer and the bottom-up decay of older convective updrafts. Both effects shift the radial flow at the updraft base from inflow to outflow, increasing type 2 occurrences at the expense of type 3. These processes also yield higher base altitudes for type 2 than those of type 3.

- DL-UL (Panel IV): Type 2 updrafts dominate the frequency distributions here.

While the surrounding rainband is predominantly stratiform (as indicated by the horizontal reflectivity contours), convective updrafts still occur embedded in the larger rainband complex. These updrafts have a base altitude that is above the radial inflow layer (here 2.5 km altitude) and thus have an out-up-out pattern.

The change in the vortex-scale inflow layer depth clearly has an impact on the preferred updraft circulation type at the different shear-relative azimuths, thus demonstrating that the wind shear has a direct influence on the convective updraft circulations. Our findings also indicate that wind shear can have an indirect influence on updraft characteristics through variations in the convective behavior at different stages of the convective life cycle. The left-of-shear, downwind end of the organized rainband complex exhibits predominantly stratiform precipitation, in which, low-level latent cooling from evaporation generates a sinking cold pool of air. As a result, new convective updrafts can be triggered and sustained via cold-pool dynamics, likely forming an out-up-out circulation (Didlake et al., 2018; Yu and Didlake, 2019). In this case, the shear indirectly boosts the convective updraft frequencies, particularly in the regions where type 2 is the preferred circulation type due to the shallow inflow layer.

This study ties together the many different characteristics of convective rainband updrafts that have been documented in the literature, both in observational and modeling studies. The results help shed light on how these updraft circulations are organized and what underlying dynamics might contribute to the observed organization. These detailed rainband characterizations can help improve our fundamental understanding of TC processes such as rapid intensification or secondary eyewall formation. Future studies would benefit from utilizing more high-resolution (both temporally and spatially) observations in order to assess the ubiquity of the convective updraft patterns and behaviors seen in this study. Thermodynamic information, either through dropsondes or models, would also greatly increase the robustness of several of the arguments presented within. The relationship between the cold pool and the resulting updraft secondary circulation also needs to be further verified.

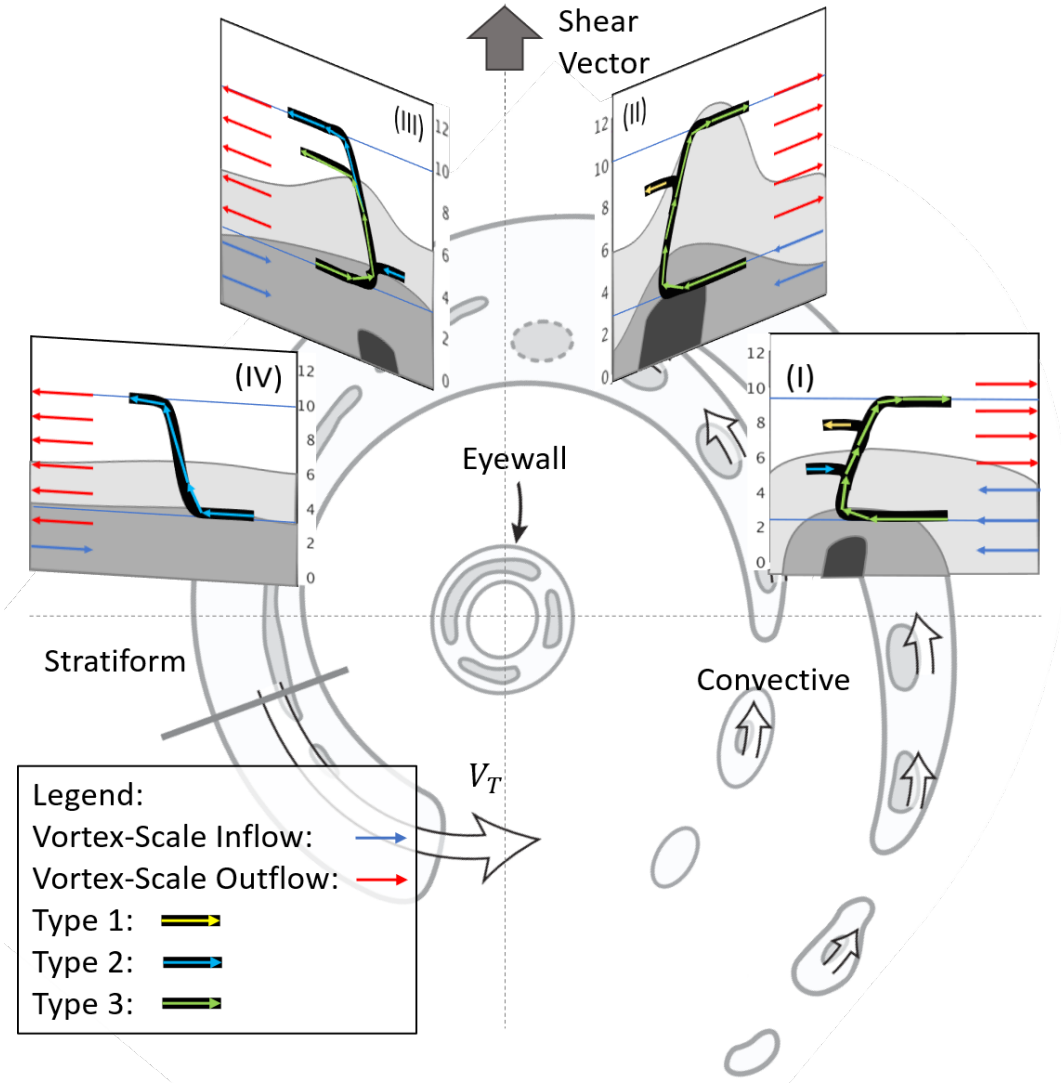

Figure 6.1. Conceptual model of convective updraft characteristics in an organized rainband complex. The plan view of the rainband complex is shown by reflectivity contours of 20 and 35 dBZ. Convective cells embedded in the rainband complex collapse (shown by the gray dashes) and form stratiform precipitation as they travel around the storm. The environmental wind shear vector points upward (gray arrow) and defines the shear-relative storm quadrants. White-filled arrows represent convective and mesoscale tangential wind jets (V_T) throughout the complex, described thoroughly in Didlake and Houze (2013a,b). Panels I-IV show radial cross sections (altitude in km) at four downshear locations. Black streamlines represent the prominent secondary circulation patterns for updrafts in these locations, with colored arrows overlaid that indicate the circulation types 1-3. Red and blue arrows on at the panel edge show the vortex-scale inflow and outflow. Reflectivity contours are drawn at 20, 30, and 35 dBZ. Adapted from Didlake and Houze (2013b).

Bibliography

Barnes, G. M., J. F. Gamache, M. A. Lemone, and G. J. Stossmeister, 1991: A convective cell in a hurricane rainband. *Monthly Weather Review*, **119 (3)**, 776–794, doi:10.1175/1520-0493(1991)119<0776:ACCIAH>2.0.CO;2.

Barnes, G. M., and M. D. Powell, 1995: Evolution of the Inflow Boundary Layer of Hurricane Gilbert (1988). **123 (8)**, 2348–2368, doi:10.1175/1520-0493(1995)123<2348:eotibl>2.0.co;2.

Barnes, G. M., and G. J. Stossmeister, 1986: The structure and decay of a rainband in Hurricane Irene (1981). *Monthly Weather Review*, **114 (12)**, 2590–2601, doi:10.1175/1520-0493(1986)114<2590:TSADOA>2.0.CO;2.

Barnes, G. M., E. J. Zipser, D. Jorgensen, and F. Marks, 1983: Mesoscale and convective structure of a hurricane rainband. *Journal of the Atmospheric Sciences*, **40 (9)**, 2125–2137, doi:10.1175/1520-0469(1983)040<2125:MACSOA>2.0.CO;2.

Bender, M. A., 1997: The effect of relative flow on the asymmetric structure in the interior of hurricanes. *Journal of the Atmospheric Sciences*, **54 (6)**, 703–724, doi:10.1175/1520-0469(1997)054<0703:TEORFO>2.0.CO;2.

Bogner, P. B., G. M. Barnes, and J. L. Franklin, 2000: Conditional instability and shear for six hurricanes over the Atlantic Ocean. *Weather and Forecasting*, **15 (2)**, 192–207, doi:10.1175/1520-0434(2000)015<0192:CIASFS>2.0.CO;2.

Bu, Y. P., R. G. Fovell, and K. L. Corbosiero, 2017: The influences of boundary layer mixing and cloud-radiative forcing on tropical cyclone size. *Journal of the Atmospheric Sciences*, **74 (4)**, 1273–1292, doi:10.1175/JAS-D-16-0231.1.

Chen, Y., and M. K. Yau, 2001: Spiral Bands in a Simulated Hurricane. Part I: Vortex Rossby Wave Verification. *Journal of the Atmospheric Sciences*, **58 (15)**, 2128–2145, doi:10.1175/1520-0469(2001)058<2128:SBIASH>2.0.CO;2.

Corbosiero, K. L., and J. Molinari, 2002: The effects of vertical wind shear on the distribution of convection in tropical cyclones. *Monthly Weather Review*, **130 (8)**, 2110–2123, doi:10.1175/1520-0493(2002)130<2110:TEOVWS>2.0.CO;2.

Corbosiero, K. L., and J. Molinari, 2003: The relationship between storm motion, vertical wind shear, and convective asymmetries in tropical cyclones. *Journal of the Atmospheric Sciences*, **60 (2)**, 366–376, doi:10.1175/1520-0469(2003)060<0366:TRBSMV>2.0.CO;2.

Corbosiero, K. L., J. Molinari, A. R. Aiyyer, and M. L. Black, 2006: The structure and evolution of Hurricane Elena (1985). Part II: Convective asymmetries and evidence for vortex rossby waves. *Monthly Weather Review*, **134 (11)**, 3073–3091, doi:10.1175/MWR3250.1.

Dai, Y., S. J. Majumdar, and D. S. Nolan, 2019: The outflow-rainband relationship induced by environmental flow around tropical cyclones. *Journal of the Atmospheric Sciences*, **76 (7)**, 1845–1863, doi:10.1175/JAS-D-18-0208.1.

Davis, C., C. Snyder, and A. C. Didlake, 2008: A vortex-based perspective of eastern Pacific tropical cyclone formation. *Monthly Weather Review*, **136 (7)**, 2461–2477, doi:10.1175/2007MWR2317.1.

Didlake, A. C., and R. A. Houze, 2009: Convective-scale downdrafts in the principal rainband of hurricane Katrina (2005). *Monthly Weather Review*, **137 (10)**, 3269–3293, doi:10.1175/2009MWR2827.1.

Didlake, A. C., and R. A. Houze, 2011: Kinematics of the secondary eyewall observed in Hurricane Rita (2005). *Journal of the Atmospheric Sciences*, **68 (8)**, 1620–1636, doi:10.1175/2011JAS3715.1.

Didlake, A. C., and R. A. Houze, 2013a: Convective-scale variations in the inner-core rainbands of a tropical cyclone. *Journal of the Atmospheric Sciences*, **70 (2)**, 504–523, doi:10.1175/JAS-D-12-0134.1.

Didlake, A. C., and R. A. Houze, 2013b: Dynamics of the stratiform sector of a tropical cyclone rainband. *Journal of the Atmospheric Sciences*, **70 (7)**, 1891–1911, doi:10.1175/JAS-D-12-0245.1.

Didlake, A. C., P. D. Reasor, R. F. Rogers, and W. C. Lee, 2018: Dynamics of the transition from Spiral Rainbands to a secondary eyewall in Hurricane Earl (2010). *Journal of the Atmospheric Sciences*, **75 (9)**, 2909–2929, doi:10.1175/JAS-D-17-0348.1.

Fischer, M. S., R. F. Rogers, and P. D. Reasor, 2019: The rapid intensification and eyewall replacement cycles of Hurricane Irma (2017). *Monthly Weather Review*, **148 (3)**, 981–1004, doi:10.1175/MWR-D-19-0185.1.

Frank, W. M., and E. A. Ritchie, 1999: Effects of environmental flow upon tropical cyclone structure. *Monthly Weather Review*, **127 (9)**, 2044–2061, doi:10.1175/1520-0493(1999)127<2044:EOEFUT>2.0.CO;2.

Frank, W. M., and E. A. Ritchie, 2001: Effects of vertical wind shear on the intensity and structure of numerically simulated hurricanes. *Monthly Weather Review*, **129 (9)**, 2249–2269, doi:10.1175/1520-0493(2001)129<2249:EOVWSO>2.0.CO;2.

Gamache, J. F., 1997: Evaluation of a fully three-dimensional vari- ational Doppler analysis technique. *28th Conf. on Radar Meteorology*.

Gao, J., M. Xue, A. Shapiro, and K. K. Droegemeier, 1999: A variational method for the analysis of three-dimensional wind fields from two Doppler radars. *Monthly Weather Review*, **127 (9)**, 2128–2142, doi:10.1175/1520-0493(1999)127<2128:AVMFTA>2.0.CO;2.

Hence, D. A., and R. A. Houze, 2008: Kinematic structure of convective-scale elements in the rainbands of hurricanes Katrina and Rita (2005). *Journal of Geophysical Research Atmospheres*, **113 (15)**, 1–20, doi:10.1029/2007JD009429.

Hence, D. A., and R. A. Houze, 2012: Vertical structure of tropical cyclones with concentric eyewalls as seen by the TRMM precipitation radar. *Journal of the Atmospheric Sciences*, **69 (3)**, 1021–1036, doi:10.1175/JAS-D-11-0119.1.

Jones, S. C., 1995: The evolution of vortices in vertical shear. I: Initially barotropic vortices. *Quarterly Journal of the Royal Meteorological Society*, **121 (524)**, 821–851, doi:10.1002/qj.49712152406.

Judt, F., and S. S. Chen, 2010: Convectively generated potential vorticity in rainbands and formation of the secondary eyewall in Hurricane Rita of 2005. *Journal of the Atmospheric Sciences*, **67 (11)**, 3581–3599, doi:10.1175/2010JAS3471.1.

Landsea, C. W., and J. L. Franklin, 2013: Atlantic hurricane database uncertainty and presentation of a new database format. *Monthly Weather Review*, **141 (10)**, 3576–3592, doi:10.1175/MWR-D-12-00254.1.

Li, Q., and Y. Dai, 2020: Revisiting azimuthally asymmetric moist instability in the outer core of sheared tropical cyclones. *Monthly Weather Review*, **148 (3)**, 1297–1319, doi:10.1175/MWR-D-19-0004.1.

Li, Q., and Q. Fang, 2019: Buoyancy of convective-scale updrafts in the outer cores of sheared tropical cyclones. *Atmospheric and Oceanic Science Letters*, **12 (1)**, 58–65, doi:10.1080/16742834.2019.1548883.

Li, Q., and Y. Wang, 2012a: A comparison of inner and outer spiral rainbands in a numerically simulated tropical cyclone. *Monthly Weather Review*, **140 (9)**, 2782–2805, doi:10.1175/MWR-D-11-00237.1.

Li, Q., and Y. Wang, 2012b: Formation and quasi-periodic behavior of outer spiral rainbands in a numerically simulated tropical cyclone. *Journal of the Atmospheric Sciences*, **69 (3)**, 997–1020, doi:10.1175/2011JAS3690.1.

Li, Q., Y. Wang, and Y. Duan, 2015: Impacts of evaporation of rainwater on tropical cyclone structure and intensity-A revisit. *Journal of the Atmospheric Sciences*, **72 (4)**, 1323–1345, doi:10.1175/JAS-D-14-0224.1.

Li, Q., Y. Wang, and Y. Duan, 2017: A numerical study of outer rainband formation in a sheared tropical cyclone. *Journal of the Atmospheric Sciences*, **74 (1)**, 203–227, doi:10.1175/JAS-D-16-0123.1.

Lorsolo, S., J. Gamache, and A. Aksoy, 2013: Evaluation of the hurricane research division doppler radar analysis software using synthetic data. *Journal of Atmospheric and Oceanic Technology*, **30 (6)**, 1055–1071, doi:10.1175/JTECH-D-12-00161.1.

May, P. T., 1996: The organization of convection in the rainbands of Tropical Cyclone Laurence. **124 (5)**, 807–815, doi:10.1175/1520-0493(1996)124<0807:TOOCIT>2.0.CO;2.

Molinari, J., D. M. Romps, D. Vollaro, and L. Nguyen, 2012: CAPE in tropical cyclones. *Journal of the Atmospheric Sciences*, **69 (8)**, 2452–2463, doi:10.1175/JAS-D-11-0254.1.

Montgomery, M. T., and R. J. Kallenbach, 1997: A theory for vortex Rossby-waves and its application to spiral bands and intensity changes in hurricanes. *Quarterly Journal of the Royal Meteorological Society*, **123 (538)**, 435–465, doi:10.1256/smsqj.53809.

Moon, Y., and D. S. Nolan, 2015: Spiral rainbands in a numerical simulation of Hurricane Bill (2009). Part I: Structures and comparisons to observations. *Journal of the Atmospheric Sciences*, **72 (1)**, 164–190, doi:10.1175/JAS-D-14-0058.1.

Powell, M. D., 1990a: Boundary Layer Structure and Dynamics in Outer Hurricane Rainbands. Part I: Mesoscale Rainfall and Kinematic Structure. *American Meteorological Society*, **118 (4)**, 891–917, doi:10.1175/1520-0493(1990)118%3C0891:BLSADI%3E2.0.CO;2.

Powell, M. D., 1990b: Boundary Layer Structure and Dynamics in Outer Rainbands. Part II: Downdraft Modification and Mixed Layer Recovery. *Monthly Weather Review*, **118 (4)**, 918–938, doi:10.1175/1520-0493(1990)118%3C0918:BLSADI%3E2.0.CO;2.

Reasor, P. D., M. D. Eastin, and J. F. Gamache, 2009: Rapidly intensifying hurricane Guillermo (1997). Part I: Low-wavenumber structure and evolution. *Monthly Weather Review*, **137 (2)**, 603–631, doi:10.1175/2008MWR2487.1.

Reasor, P. D., M. T. Montgomery, and L. D. Grasso, 2004: A new look at the problem of tropical cyclones in vertical shear flow: Vortex resiliency. *Journal of the Atmospheric Sciences*, **61 (1)**, 3–22, doi:10.1175/1520-0469(2004)061<0003:ANLATP>2.0.CO;2.

Reasor, P. D., R. Rogers, and S. Lorsolo, 2013: Environmental flow impacts on tropical cyclone structure diagnosed from airborne doppler radar composites. *Monthly Weather Review*, **141 (9)**, 2949–2969, doi:10.1175/MWR-D-12-00334.1.

Ren, Y., J. A. Zhang, J. L. Vigh, P. Zhu, H. Liu, X. Wang, and J. B. Wadler, 2020: An observational study of the symmetric boundary layer structure and tropical cyclone intensity. *Atmosphere*, **11 (2)**, doi:10.3390/atmos11020158.

Riemer, M., and M. T. Montgomery, 2011: Simple kinematic models for the environmental interaction of tropical cyclones in vertical wind shear. *Atmospheric Chemistry and Physics*, **11 (17)**, 9395–9414, doi:10.5194/acp-11-9395-2011.

Rogers, R., S. Chen, J. Tenerelli, and H. Willoughby, 2003: A numerical study of the impact of vertical shear on the distribution of rainfall in Hurricane Bonnie (1998). *Monthly Weather Review*, **131 (8)**, 1577–1599, doi:10.1175//2546.1.

Rogers, R., S. Lorsolo, P. Reasor, J. Gamache, and F. Marks, 2012: Multiscale analysis of tropical cyclone kinematic structure from airborne doppler radar composites. *Monthly Weather Review*, **140 (1)**, 77–99, doi:10.1175/MWR-D-10-05075.1.

Rogers, R., P. Reasor, and S. Lorsolo, 2013: Airborne doppler observations of the inner-core structural differences between intensifying and steady-state tropical cyclones. *Monthly Weather Review*, **141 (9)**, 2970–2991, doi:10.1175/MWR-D-12-00357.1.

Rozoff, C. M., D. S. Nolan, J. P. Kossin, F. Zhang, and J. Fang, 2012: The roles of an expanding wind field and inertial stability in tropical cyclone secondary eyewall formation. *Journal of the Atmospheric Sciences*, **69 (9)**, 2621–2643, doi:10.1175/JAS-D-11-0326.1.

Rozoff, C. M., W. H. Schubert, B. D. McNoldy, and J. P. Kossin, 2006: Rapid filamentation zones in intense tropical cyclones. *Journal of the Atmospheric Sciences*, **63 (1)**, 325–340, doi:10.1175/JAS3595.1.

Ryan, B. F., G. M. Barnes, and E. J. Zipser, 1992: A Wide Rainband in a Developing Tropical Cyclone. *Monthly Weather Review*, **120 (3)**, 431–447, doi:10.1175/1520-0493(1992)120%3C0431:AWRIAD%3E2.0.CO;2.

Samsury, C. E., and E. J. Zipser, 1995: Secondary Wind Maxima in Hurricanes: Airflow and Relationship to Rainbands. *Monthly Weather Review*, **123 (12)**, 3502–3517, doi:10.1175/1520-0493(1995)123%3C3502:SWMIHA%3E2.0.CO;2.

Sawada, M., and T. Iwasaki, 2010a: Impacts of evaporation from raindrops on tropical cyclones. Part I: Evolution and axisymmetric structure. *Journal of the Atmospheric Sciences*, **67 (1)**, 71–83, doi:10.1175/2009JAS3040.1.

Sawada, M., and T. Iwasaki, 2010b: Impacts of evaporation from raindrops on tropical cyclones. Part II: Features of rainbands and asymmetric structure. *Journal of the Atmospheric Sciences*, **67 (1)**, 84–96, doi:10.1175/2009JAS3195.1.

Smith, R. K., M. T. Montgomery, and N. V. Sang, 2009: Tropical cyclone spin-up revisited. *Quarterly Journal of the Royal Meteorological Society*, **135 (642)**, 1321–1335, doi:10.1002/qj.428.

Steiner, M., R. a. Houze Jr., and S. E. Yuter, 1995: Climatological Characteracterization of Three-Dimensional Storm Structure from Operational Radar and Rain Gauge Data. *Journal of Applied Meteorology*, **34 (9)**, 1978–2007, doi:10.1175/1520-0450(1995)034%3C1978:CCOTDS%3E2.0.CO;2.

Tang, X., W. C. Lee, and M. Bell, 2014: A squall-line-like principal rainband in Typhoon Hagupit (2008) observed by airborne Doppler radar. *Journal of the Atmospheric Sciences*, **71 (7)**, 2733–2746, doi:10.1175/JAS-D-13-0307.1.

Tang, X., W. C. Lee, and M. Bell, 2018: Subrainband structure and dynamic characteristics in the principal rainband of Typhoon Hagupit (2008). *Monthly Weather Review*, **146 (1)**, 157–173, doi:10.1175/MWR-D-17-0178.1.

Terwey, W. D., and C. M. Rozoff, 2014: Objective convective updraft identification and tracking: Part 1. Structure and thermodynamics of convection in the rainband regions of two hurricane simulations. *Journal of Geophysical Research (Atmospheres)*, **119 (10)**, 6196–6206, doi:10.1002/2014JD021606.

Wadler, J. B., R. F. Rogers, and P. D. Reasor, 2018: The relationship between spatial variations in the structure of convective bursts and tropical cyclone intensification as determined by airborne Doppler radar. *Monthly Weather Review*, **146 (3)**, 761–780, doi:10.1175/MWR-D-17-0213.1.

Wang, Y., 2002: Vortex Rossby waves in a numerically simulated tropical cyclone. Part II: The role in tropical cyclone structure and intensity changes. *Journal of the Atmospheric Sciences*, **59 (7)**, 1239–1262, doi:10.1175/1520-0469(2002)059<1239:VRWIAN>2.0.CO;2.

Willoughby, H. E., and M. B. Chelmow, 1982: Objective Determination of Hurricane Tracks from Aircraft Observations. *Monthly Weather Review*, **110 (9)**, 1298–1305, doi:10.1175/1520-0493(1982)110<1298:odohtf>2.0.co;2.

Willoughby, H. E., J. A. Clos, and M. G. Shoreibah, 1982: Concentric Eye Walls, Secondary Wind Maxima, and The Evolution of the Hurricane Vortex. *Journal of the Atmospheric Sciences*, **39 (2)**, 395–411, doi:10.1175/1520-0469(1982)039%3C0395:CEWSWM%3E2.0.CO;2.

Willoughby, H. E., F. D. Marks, and R. H. Feinberg, 1984: Stationary and moving convective bands in hurricanes. **41 (22)**, 3189–3211, doi:10.1175/1520-0469(1984)041<3189:SAMCBI>2.0.CO;2.

Wingo, M. T., and D. J. Cecil, 2010: Effects of vertical wind shear on tropical cyclone precipitation. *Monthly Weather Review*, **138 (3)**, 645–662, doi:10.1175/2009MWR2921.1.

Yu, C. K., and Y. Chen, 2011: Surface fluctuations associated with tropical cyclone rainbands observed near Taiwan during 2000-08. *Journal of the Atmospheric Sciences*, **68 (8)**, 1568–1585, doi:10.1175/2011JAS3725.1.

Yu, C. K., C. Y. Lin, L. W. Cheng, J. S. Luo, C. C. Wu, and Y. Chen, 2018: The degree of prevalence of similarity between outer tropical cyclone rainbands and squall lines. *Scientific Reports*, **8 (1)**, 1–15, doi:10.1038/s41598-018-26553-8.

Yu, C. K., and C. L. Tsai, 2013: Structural and surface features of arc-shaped radar echoes along an outer tropical cyclone rainband. *Journal of the Atmospheric Sciences*, **70 (1)**, 56–72, doi:10.1175/JAS-D-12-090.1.

Yu, C. L., and A. C. Didlake, 2019: Impact of stratiform rainband heating on the tropical cyclone wind field in idealized simulations. *Journal of the Atmospheric Sciences*, **76 (8)**, 2443–2462, doi:10.1175/JAS-D-18-0335.1.

Yu, C. L., A. C. Didlake, F. Zhang, and R. G. Nystrom, 2020: Asymmetric rainband processes leading to secondary eyewall formation in a model simulation of Hurricane Matthew (2016). *Journal of the Atmospheric Sciences*, in press, doi:10.1175/JAS-D-20-0061.1.

Zhang, J. A., R. F. Rogers, P. D. Reasor, E. W. Uhlhorn, and F. D. Marks, 2013: Asymmetric hurricane boundary layer structure from dropsonde composites in relation to the environmental vertical wind shear. *Monthly Weather Review*, **141 (11)**, 3968–3984, doi:10.1175/MWR-D-12-00335.1.